Stony Brook University

OFFICIAL COPY

The official electronic file of this thesis or dissertation is maintained by the University Libraries on behalf of The Graduate School at Stony Brook University.

© All Rights Reserved by Author.

Studies on X-ray Diffraction Microscopy

A Dissertation Presented

by

Huijie Miao

to

The Graduate School

in Partial Fulfillment of the Requirements

for the Degree of

Doctor of Philosophy

in

Physics

Stony Brook University

August 2008

Stony Brook University

The Graduate School

Huijie Miao

We, the dissertation committee for the above candidate for the Doctor of Philosophy degree, hereby recommend acceptance of this dissertation.

Chris Jacobsen – Dissertation Advisor
Professor, Department of Physics and Astronomy

Thomas Kuo – Chairperson of Defense
Professor, Department of Physics and Astronomy

Laszlo Mihaly
Professor, Department of Physics and Astronomy

Qun Shen
Senior Scientist, Brookhaven National Laboratory

This dissertation is accepted by the Graduate School.

Lawrence Martin
Dean of the Graduate School

Abstract of the Dissertation

Studies on X-ray Diffraction Microscopy

by

Huijie Miao

Doctor of Philosophy

in

Physics

Stony Brook University

2008

This dissertation includes three main parts: studies on coherence requirements for the diffraction microscopy experiments, ice formation on frozen-hydrated sample during data collection, and centering of the diffraction data sets. These three subjects are all in support of our groups overall goal of high resolution 3D imaging of frozen hydrated eukaryotic cells via x-ray diffraction microscopy.

X-ray diffraction microscopy requires coherent illumination. However, the actual degree of coherence at some beamlines has never been tested. In research on coherence, our first aim is to determine the transverse coherence width at the sample plane at BL 9.0.1 at the Advanced Light Source in Lawrence Berkeley National Labo-

ratory. An analytical calculation of the coherence at the sample plane is presented. Experimental diffraction patterns of pinhole-pair samples were also taken at the beamline to determine the coherence. Due to the irregular shape of the pinholes and other optics complexity, it was very difficult to fit the data with known theoretical equations as it was traditionally done with 1D data. However, we found out that the auto-correlation function shows clearly three spots. Theoretical calculation have been carried out to show that the degree of coherence can be obtained from the intensities of the three spots. These results are compared with the results from the analytical calculation. We then perform a simulation, showing the required transverse coherence width for reconstructing samples with a given size.

Ice accumulation has been a major problem in X-ray diffraction microscopy with frozen hydrated samples. Since the ice structure is different from point to point, we cannot subtract the scattering from ice, nor assume a completely "empty" region outside the finite support constraint area as required for reconstruction. Ice forms during the sample preparation and transfer. However, from the tests we did in September 2007, we found that the ice layer thickens significantly during the data collecting process. One of the tests we did was putting a dry room-temperature grid into the beam, cooling it down to liquid nitrogen temperature, and then collecting the diffraction pattern of it over time. This test showed that, after

the cold grid remained in the chamber for a while, a ring could be observed in the diffraction pattern. The time necessary for this ring to be visible is highly dependent on the pressure and vacuum history of the chamber. We will discuss how the chamber pressure influences the ice accumulation rate, how an anti-contamination device can help to reduce the rate, and how this ring forms.

The last part of the research is based on simulations and a real data set collected on beamline 9.0.1 at the ALS in Berkeley. In X-ray diffraction microscopy, one of the major challenges when processing the data is to accurately determine the true center of the recorded data; that is, the zero spatial frequency position. Simulations of reconstructing shifted data show that if the center of a 2D diffraction pattern is shifted by more than 3 pixels from its true center, the positivity constraint to the phase, which otherwise might be applied to improve the convergence of the reconstruction algorithm, cannot be imposed. Moreover, the phase unwrapping problem may appear during the reconstruction. These issues undermine the quality of the reconstruction of 2D data. Furthermore, the individual shift in each 2D pattern will lead to errors when assembling a 3D diffraction data cube, making the 3D reconstruction very difficult. We developed a method which uses power spectra of the partial diffraction pattern to pre-align the data. A reconstruction without severe phase unwrapping can then be obtained from the pre-aligned data. Next, the precise zero spatial frequency

position can be found by examining the linear ramp present in the reconstructed phase. This method was applied to a freeze-dried yeast data set to show that this approach is effective with experimental data.

To my parents and Simone.

Contents

List of Figures

List of Tables

Acknowledgements

Believe it or not, this is the day I start writing my dissertation. I can't help writing this part today! I've been looking forward to this moment for long, since I am really not very good at expressing my gratitude to others, and I missed many opportunities to say "thank you" in life. Hope those to whom I own one find one here.

The first "thank you" is to my dissertation advisor Prof. Chris Jacobsen. He has been a spiritual model for me in work and in life. He showed me how efficient one can possibly be, and how busy one can possibly be. He taught me the way to socialize with others, the way to express my ideas in a more objective way. I haven't mastered the art yet, but I will work hard towards the direction. I wish I had spent more time with him discussing problems related and unrelated to work. Here, I would like to give a big "thanks" to him for all his help.

Another person who had a huge impact on me is Prof. Janos Kirz. Thinking about him often makes me emotional. His enthusiasm to work truly touches me. When we have night-shifts, he has night-shifts; when we share 16-hour shifts, he takes the whole 16-hour shifts! No matter how occupied he is with his other responsibilities, he will always show up at the beamline. Once we

told him not to come for one night after several continuous night shifts, and he replied, “I am just so interested in the experiments!” He is also a very kind man. I will never forget his generosity, his humor and his wit.

In Chinese, we say be your teacher for one day; be your father for life. I respect my two great teachers for life.

One of the factors made this journey really enjoyable and unforgettable is my colleagues. Among them, I talked most with Xiaojing Huang. We are both Chinese and also worked closely on many projects. We spent many days and nights together in the thunder of the beamline pumps, we rode together to school and back every week after I moved to Boston. There were many interesting and inspiring conversations with him. I am very grateful to his company and free rides. I feel lucky to be in this wonderful group. I still remember the big smile on Tobi’s face when he first welcomed me to the group as a big brother; I appreciate Holger’s candid comments on almost everything (and his interesting explanation of the origin of the word “cappuccino”, a small cup! Although it can’t be right, since cup in Italian is “tazza”, not “cappu”, it is still really cute and creative.); I also enjoy very much discussing problems with David, Joshua, Andy, Ben and Ming, they are so knowledgeable and patient. I am glad that we had always a “big” population of females in the group. Enju, Mirna, Bjorg and Johanna, thanks for the feminine little discussions and girls’ lunches. A special thanks to Sue, who is always ready to help, no matter at the beamline or at the BBQ battlefield. Jan, Christian and Simon are the rookies of the group. I am very impressed by Christian’s neatest way to cut birthday cakes (so precisely that nobody would worry about getting one molecule less). I am amazed by how much beer Jan can handle in

two hours. I am looking forward to witness Simon's dancing skill. Thanks all for being part of the happiness.

I wish to take this opportunity to thank another two persons who have helped me much. One is Stefano, who worked with me closely on the coherence project. Every discussion with him enlightens me. Another one is Kai, who generously offered me hospitality during the last year of my study. He made his room available to me whenever I needed it. I will surely cherish our friendship.

I have to thank my parents for being supportive all the time. They were brave enough to let me come to the US for a PhD. Thanks for their endless care and support. Without you, there would be no me (...no wonder!).

Finally, my biggest "thanks" goes to my husband, Simone. You support a sky for me!

Chapter 1

Introduction

Lensless imaging involves coherent illumination of a non-repetitive specimen, collection of the diffracted wave, and numerical reconstruction of an image based on constraints. In our case, 520 eV to 750 eV X-rays are used to image frozen-hydrated or freeze-dried biological samples. The experiments are done at beamline 9.0.1, at the Advanced Light Source (ALS) in Lawrence Berkeley National Lab (LBNL). The beamline plus the experimental chamber and the reconstruction algorithm comprises an X-ray diffraction microscope, which differs from a conventional microscope in that there is no objective lens. The iterative reconstruction algorithm together with the CCD camera act to take the place of the objective lens, which translate the pattern in reciprocal space into a real space image. The advantage of imaging without lenses is that the reconstructed image is loss-free, which means its resolution is given only by the diffraction and dose limit [2]. In this chapter we are going to briefly evaluate the method, review the history of the developments and discuss some of the challenges.

1.1 The Advantages and Problems of Lensless Imaging

1.1.1 Why Lens-less?

The resolution of the lensless imaging depends solely on the limitation of collected diffraction data and radiation damage. Is this resolution going to be better than that of conventional lens imaging? This is an especially big consideration when imaging biological samples which have a low tolerance of radiation. In conventional microscopy, the photon beam diffracted by the specimen is collected and phased by lens which leads to a real-space image of the specimen. Due to the finite numerical aperture cutoffs and modest efficiencies of x-ray focusing lens, *i.e.*, the zone plate, the real-space image has a limited resolution.

To better understand the issue of which type of microscopy delivers a higher resolution image within a given exposure limit, our group undertook a simulation study to which I contributed and which is being written up by Xiaojing Huang [3]. To evaluate x-ray diffraction microscopy, we simulate coherent illumination of a cell-like protein object in ice, calculate its diffraction intensity with photon noise, and use the iterative algorithm to reconstruct the image of the "cell." To render an image of conventional microscopy, we calculate the absorption profile of the same "cell," convolve it with the point spread function of a representative soft x-ray zone plate, take efficiency of the zone plate into account, and add the photon noise. To accurately evaluate the resolution of the images, we adopted a signal-to-noise ratio (SNR) concept used by Glaeser

[4] and Sayre [5]. The SNR of a given image is calculated from the correlation coefficient of different copies of the same image [6].

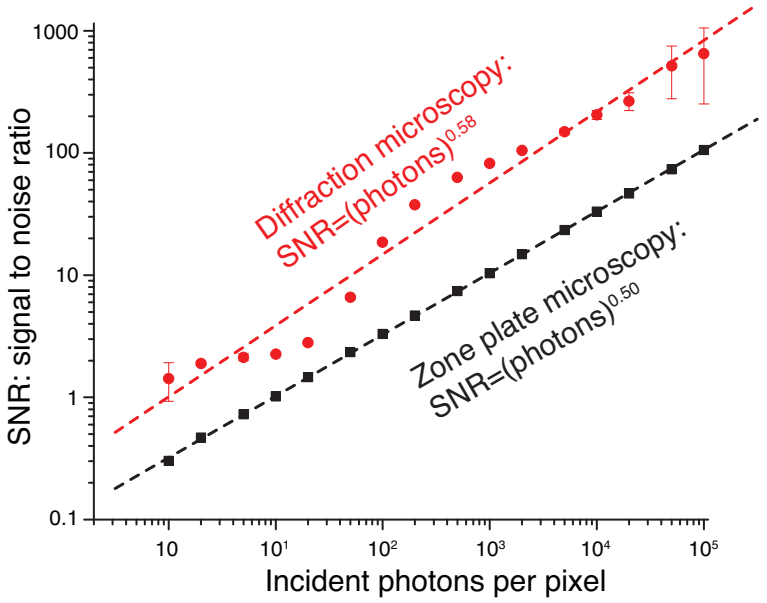

Figure 1.1: Simulation of image signal to noise (SNR) in diffraction microscopy reconstructions (red) and full-field imaging with a 20 nm outermost zone width zone plate with 10% efficiency. In both cases a simulated cell-like protein object in ice was considered, and Poisson noise was inserted on the "recorded" intensity. The 5-fold improvement in SNR observed in these simulations is consistent with the 25-fold improvement in data detection efficiency at high spatial frequencies and the relationship that SNR is proportional to $\sqrt{\text{photons}}$. Calculation by X. Huang *et al.*, Stony Brook, and presented at the Coherence 2007 meeting in Asilomar.

The results of the simulations are shown in Fig. 1.1. Since the SNR is proportional to $\sqrt{\text{photons}}$, the 5-fold improvement in SNR observed in the simulations is consistent with the hundred-fold improvement in data detection efficiency at high spatial frequencies. As the incident photon number per pixel varies from 10 to 10^5, the SNR of the image obtained with diffraction microscopy is always significantly higher than that of the zone-plate image.

This confirms the motivation of the research on x-ray diffraction microscopy: imaging with higher resolution.

1.1.2 The Phase Problem

The far-field radiation distribution from a scattering object can often be written within two limiting approximations: the Fresnel approximation and the Fraunhofer approximation. Fresnel diffraction assumes spherical wave propagation, which can be applied when the Fresnel number is $F \geq 1$. The Fresnel number is defined as $F = \frac{a^2}{L\lambda}$, where a is the size of the object, L is the distance between object and the observation plane, and λ is the wavelength. The exit wave from the object is called the "near-field" diffraction pattern, which is given by the Fresnel diffraction integral

$$U(x,y) = \frac{e^{\imath kz}}{\imath\lambda z} \iint_{-\infty}^{\infty} U(\xi,\eta) e^{\imath \frac{k}{2z}[(x-\xi)^2+(y-\eta)^2]} \, d\xi d\eta \,, \tag{1.1}$$

where ξ and η are the coordinates in the object plane, x and y are the coordinates in the observation plane, z is the wave propagation direction, k is the wave number, and U is the electromagnetic wave field [7].

On the other hand, Fraunhofer diffraction assumes plane wave propagation, which occurs when $F \ll 1$, namely the distance between the object and the observation plane is much bigger than the object size. The resulting pattern is then called the "far-field" diffraction pattern, which can be written in the form of a Fourier transform [7]

$$U(f_x,f_y) = \frac{e^{\imath kz} e^{\imath\pi\lambda z(f_x^2+f_y^2)}}{\imath\lambda z} \iint_{-\infty}^{\infty} U(\xi,\eta) e^{2\pi\imath(f_x\xi+f_y\eta)} \, d\xi d\eta \,. \tag{1.2}$$

where

$$f_x = \frac{x}{\lambda z} \qquad \text{and} \qquad f_y = \frac{y}{\lambda z} \tag{1.3}$$

are referred to as spatial frequencies. The integral part is simply the Fourier transform of the object distribution, evaluated at frequencies f_x and f_y. However, in x-ray diffraction microscopy only the intensity of the diffraction pattern is recorded, so that the phase has been lost. If the "full" diffraction pattern (including magnitude and phase) is known, according to Eq. 1.2, an inverse Fourier transform may reveal the image of the object. But in reality, it is often difficult to retrieve the phase in the far-field diffraction pattern. This is known in the field as "the phase problem."

To illustrate the important role phase plays in the retrieval of real-space image, we show the effect of exchanging the phases of two diffraction patterns in Fig. 1.2. On the top left is the picture of Ylan (my seven-months old niece) and on the top right is the picture of Milù (a Chartreux cat of one of my friends). If we do a Fourier transform on both pictures, keep the magnitudes and exchange the phases, and then do an inverse Fourier transform, what we get are the pictures shown at the bottom of Fig. 1.2. Surprisingly, after combining Ylan's magnitude with Milù's phase, what we see is essentially the cat; the combination of Milù's magnitude and Ylan's phase leads to features of the baby. This simple exercise shows that the phase is indeed essential in imaging retrieval processes. Without successfully recovering the phase, it is impossible to reconstruct the correct image in real space.

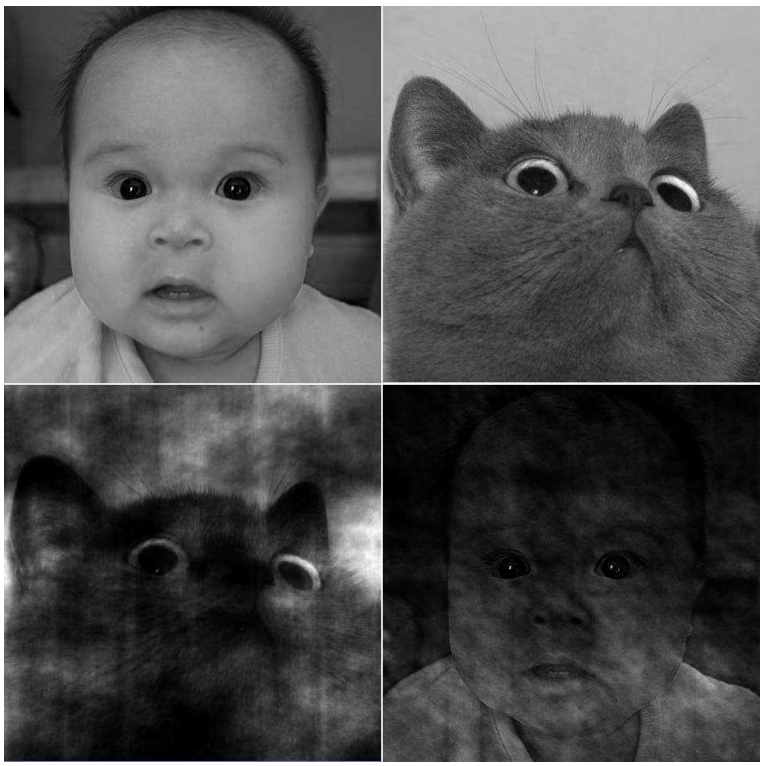

Figure 1.2: Illustration of the importance of Fourier plane phase in image reconstruction. At top are shown two images: one of my niece Ylan (left), and one of my friends cat Milù (right). At bottom are shown two images where the Fourier plane magnitudes of one image were combined with the Fourier plane phases of the other. At bottom left, Ylan's Fourier magnitude is combined with Milù's phases. At bottom right, Milù's Fourier magnitude is combined with Ylan's phase.

1.2 Brief History and Recent Developments in the Field

1.2.1 X-ray Crystallography

The idea of using x-ray to determine the structure of crystals was proposed and later experimentally proved by von Laue in 1912, for which he was awarded the Nobel Prize in Physics in 1914.

Crystals are solids with identical repeated unit cells. When x-rays impinge on a crystal sample, they are scattered mainly by the electrons in the crystal. Within Born approximation, the far field diffraction intensity is the Fourier transform of the electron density function, as we discussed in Eq. 1.2. If we denote the electron density function of the unit cell as $U(x, y)$, and the one of the crystal lattice as $L(x, y)$, the structure of a crystal is then the convolution of the unit cell structure with the lattice structure, namely $U(x, y) * L(x, y)$, where $*$ indicates that a two-dimensional convolution is to be performed. The Fourier convolution theorem states that the Fourier transform of a convolution of two functions is equal to the product of the Fourier transform of each, or

$$\mathcal{F}\{U(x, y) * L(x, y)\} = \mathcal{F}\{U(x, y)\}\mathcal{F}\{L(x, y)\}\,. \tag{1.4}$$

Thus, the diffraction pattern of a crystal can be expressed as the product of the diffraction pattern of a unit cell and that of the lattice. This implies that the diffraction pattern of a crystal has intensity only on Bragg peaks, and it is empty everywhere else.

Before moving on to the discussion of modern phase retrieval developments in crystallography, we are going to briefly review a fundamental result in the field, which is known as the "Whittaker-Shannon sampling theorem." The theorem states that the exact recovery of a bandlimited function $g(x, y)$ can be achieved from an appropriately spaced rectangular array of its sampled values; the recovery is accomplished by injecting, at each sampling point, an interpolation function consisting of a product of sinc functions (because $\mathrm{sinc}(x) = \frac{\sin \pi x}{\pi x}$ is the Fourier transform of a rectangle function), where each interpolation function is weighted according to the sampled value of g at the corresponding point [7]

$$g(x,y) = \sum_{n=-\infty}^{\infty} \sum_{m=-\infty}^{\infty} g\Big(\frac{n}{2B_x}, \frac{m}{2B_y}\Big) \mathrm{sinc}\Big[2B_x\Big(x - \frac{n}{2B_x}\Big)\Big] \mathrm{sinc}\Big[2B_y\Big(y - \frac{m}{2B_y}\Big)\Big]. \tag{1.5}$$

Since g is bandlimited, its spectrum G is nonzero over only a finite region R of the frequency space. B_x and B_y here stand for the half width in the f_x and f_y directions, respectively, of the smallest rectangle that completely encloses the region R.

Following the Shannon's sampling law Eq. 1.5, in 1952, D. Sayre concluded that only when the phase at Bragg peaks is determined, the unit cell structure of the crystal can be solved [8]. There were a lot of developments on the determination of the phases at Bragg peaks using known structural information since then. An important example is the emergence of the so-called "direct methods." In this class of methods, probability relationships applied to the phases of the most intense diffraction peaks were used to link the diffraction pattern with the known molecular models to solve the structure. Some con-

straints on the phase can be applied to restrict its possible values and allow initial estimates and refinements. The facts that scattering centers (atoms) in a crystal are discrete and that the electron density of the sample is non-negative are examples of such constraints. A number of inequality relationships based on various constraints were developed [8–10], and led to important applications [11].

In 1953, the DNA structure was determined using precise molecular model-building along with its diffraction data, as shown in Fig. 1.3. Watson, Crick and Wilkins were awarded the Nobel Prize in Physiology or Medicine in 1962 for their outstanding contribution in this work. Although chemical insight and model building were essential in resolving the structure, the inferences from x-ray diffraction data helped greatly to achieve the success. Another major milestone was the solution of more general globular proteins by Perutz and Kendrew who shared the Nobel Prize in chemistry in 1962. Their original way to interpret the x-ray diffraction data was to carefully label the proteins with heavy atoms such as mercury (Hg), looking for the strong scattering from the heavy atoms to infer the structure of the protein molecules. X-ray diffraction crystallography has had much success in applications in chemistry, material science and biology since then. The most recent interest has been focused on solving complex protein structures.

1.2.2 Diffraction Microscopy

X-ray crystallography is a well established method for recovering the electron density within an average unit cell of a crystal. However, unlike crystal

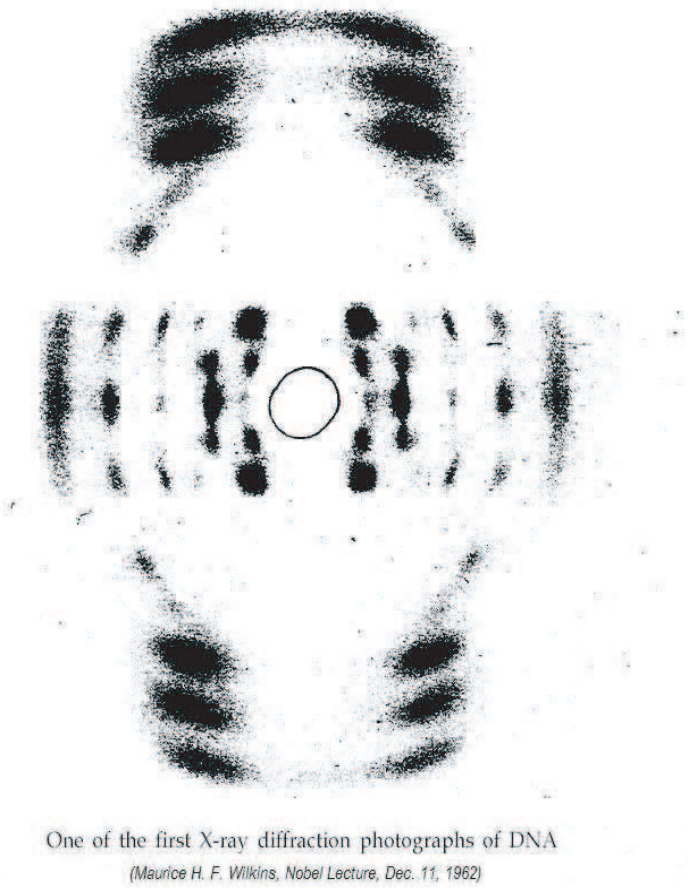

Figure 1.3: One of the first diffraction photographs of DNA molecules. This figure is reproduced from Wilkins. [1].

specimens, the diffraction intensity of a non-crystalized sample presents a continuous distribution. There are no Bragg peaks and little a priori structural information. In 1980, Sayre first proposed the idea to extend crystallography to non-crystalized samples [12]. The continuous pattern makes oversampling possible. Shannon's sampling theorem tells us that it is possible to retrieve the phase information from over-sampled magnitudes. The idea of recovering Fourier magnitudes from far-field diffraction data goes back to Fienup in 1978 [13], where he explored the oversampling ratio. In 1998, Miao confirmed with simulations that a successful reconstruction requires the oversampling ratio to be at least 2.5 [14]. Later on, various research groups tried to realize the idea in experiments. The first demonstration was done by Miao in 1999 [15], in which he successfully reconstructed the first six English alphabet letters made of gold dots. The resolution was estimated to be 75 nm. More achievements with material science specimens have been reported [16–19]. In 2005, our group had reconstructed the first image of a freeze-dried eukaryotic cell, a yeast cell [20]. This is a milestone in the journey, which directs our future research onto frozen hydrated biological samples.

1.2.3 Phase Retrieval Algorithms

When recording the diffraction intensity, the phase is lost. The major obstacle in realizing diffraction microscopy is to develop the methods to retrieve the phase from the measured magnitude. There were four types of algorithm developed in the field over the time, pioneered by Gerchberg-Saxton's Error Reduction Algorithm (ER) [21], Fienup's Basic Input-Output Algorithm

(BIO), Fienup's Hybrid Input-Output Algorithm (HIO) [22], and advanced by Luke's Relaxed Averaged Successive Reflector (RASR) [23]. In general, these algorithms are attempting to find the solution that satisfies all the constraints.

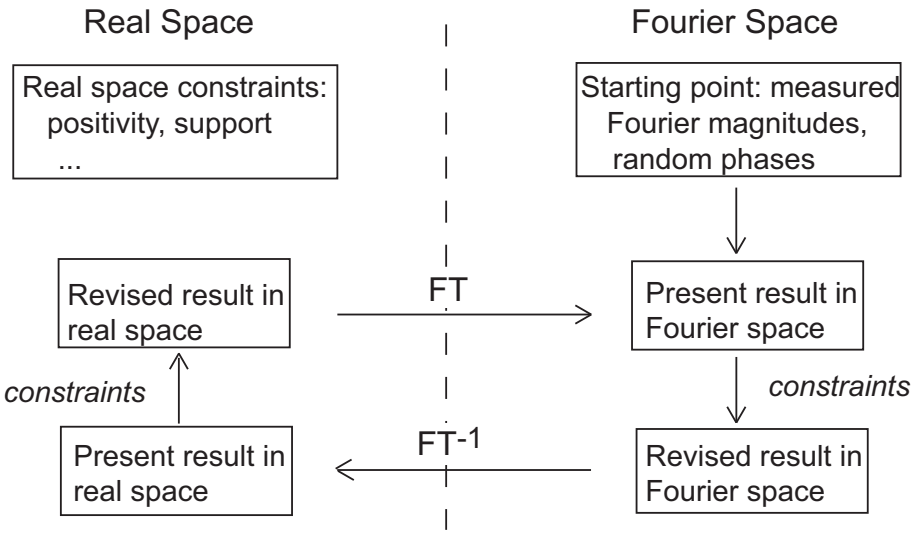

Figure 1.4: Illustration of the phase retrieval algorithm. Reconstruction starts from a random guess of the phases, combined with the measured magnitudes. Fourier space constraints and real space constraints are then applied to get a modified solution in real space.

Fig. 1.4 illustrates the typical iterative process of such reconstruction algorithm. It usually starts with a guessed diffraction pattern in the Fourier space, which is obtained by combining the measured magnitudes and random phases. After applying Fourier space constraints to modify it, we do an inverse Fourier transform to obtain the corresponding real space image. Real space constraints are then applied, and a Fourier transform is performed to get the improved version of the guessed diffraction pattern. The iterative algorithm goes on, going back and forth between Fourier space and real space, applying constraints, till the guessed diffraction magnitudes are very close to the measured ones.

An error parameter, which reflects the difference between the current guessed diffraction magnitudes and the true ones, is set to monitor progress. There are many different constraints that can be applied to a specific data. Usually the constraints in Fourier space may include the Fourier modulus constraint, which keeps the current phases and imposes the measured magnitudes. The constraints in real space may include the support constraint and the positivity constraint. The support constraint defines the region of interest. As discussed in the last section, the diffraction data has to meet the over-sampling ratio requirement which means that the field of view has to be much bigger than the sample. We take the empty background (zeros) as known parameter, so that the unknown pixels within the sample can be solved. A support is then a mask made to set the boundary of the sample. Pixels outside of the support should have zero electron density. When applying the support constraint, we keep the pixels inside the support untouched, while setting the ones outside to be zeros. In addition, a positivity constraint can be applied to ensure that electron density values are not negative. When detecting pixels with negative magnitudes, we bring them back to zero.

The difference between the four algorithms listed above is the way they apply the constraints to g_n (the current guess image at iteration n) in order to get g_{n+1} (the next improved guess image at iteration $n+1$). In the following, we list the detailed procedure used in each algorithm. We use S to denote the support, $F_{\text{mod}}()$ to represent the Fourier Modulus constraint, and β is a constant controlling the efficiency of the algorithm.

In ER,

$$g_{n+1} = \begin{cases} F_{\text{mod}}(g_n), \ g_n \subset S \\ 0, \ \text{otherwise.} \end{cases} \tag{1.6}$$

In BIO

$$g_{n+1} = \begin{cases} g_n, \ g_n \subset S \\ g_n - F_{\text{mod}}(g_n), \ \text{otherwise.} \end{cases} \tag{1.7}$$

In HIO

$$g_{n+1} = \begin{cases} g_n, \ g_n \subset S \\ g_n - \beta F_{\text{mod}}(g_n), \ \text{otherwise.} \end{cases} \tag{1.8}$$

In RASR

$$g_{n+1} = \begin{cases} g_n, \ g_n \subset S \\ (1-2\beta)F_{\text{mod}}(g_n) + \beta g_n, \ \text{otherwise.} \end{cases} \tag{1.9}$$

Recently, Elser further developed the difference map algorithm [24], which is an advanced version of HIO. In it, the update rules are

$$g_n^{(1)} = S((1+\gamma_2)F_{\text{mod}}(g_n) - \gamma_2 g_n) \tag{1.10}$$

$$g_n^{(2)} = F_{\text{mod}}((1+\gamma_1)S(g_n) - \gamma_1 g_n) \tag{1.11}$$

$$g_{n+1} = g_n + \beta(g_n^{(1)} - g_n^{(2)}), \tag{1.12}$$

where $\gamma_1 = -\frac{1}{\beta}$, $\gamma_2 = \frac{1}{\beta}$, and $S()$ applies the support constraint which sets any pixel outside of the support to be zero. When $\beta = 1.0$, difference map reduces to HIO. The difference map algorithm has been used through this dissertation

to achieve various reconstructions.

There are also other developments recently [18, 25–30], which focus on improving the efficiency and stability of the phase retrieval algorithm.

1.3 Current Challenges and Open Problems

One of the most important applications of x-ray diffraction microscopy is to image biological specimens. The functions of biological cells are largely determined by their structures, thus high resolution images of the cells are extremely informative to biologists. However, there are still obstacles on the way to achieve this type of imaging.

As mentioned in the last section, our group reconstructed a freeze-dried yeast cell in 2005. However, while freeze-dried cells are easier to collect data from, greater biological fidelity can be obtained by looking at frozen-hydrated specimens. This is illustrated in Fig. 1.5 [31] which shows the difference between a chemically fixed and dried cell and a frozen-hydrated cell. Most of the inner structures are degraded or distorted during the drying process. To image the cells in an environment closer to their living state, frozen-hydrated cells should be used. They are rapidly plunged into liquid ethane to create vitreous ice in the cells and then transferred to liquid nitrogen for storage. Because the ice matrix strengthens the structure, these cells are less likely to collapse in the beam, thus conserving a much more similar structure as that of the alive ones. Yet the painstaking efforts towards the imaging of frozen-hydrated cells have not paid off. It turned out that it is much more difficult to image frozen-hydrated cells than dried ones. The first problem lies in the sample

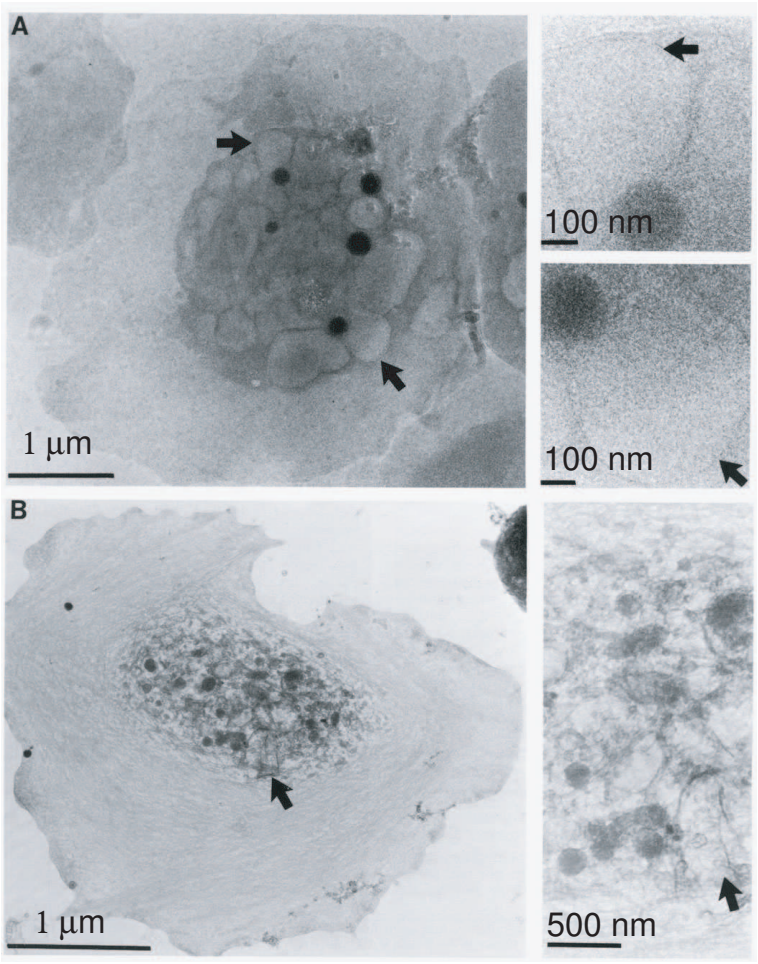

Figure 1.5: Figure from OToole et al. [31]. Human blood platelets at 1 MeV transmission electron microscope (JEOL-1000). A: frozen-hydrated; B: 2% glutaraldehyde fixed, 1% OsO4 postfixed, and critical point dried.

preparation. Because the over-sampling requirement imposes the constraint on the background of the cell, every point outside the cell boundary should have zero electron density. This is naturally satisfied with freeze-dried cells, while it is almost impossible for frozen-hydrated cells. The ice scattering in the background can be a big problem in the reconstruction. One can try to minimize the thickness and roughness of the ice layer by tuning the plunging parameters, but it can not be totally avoided. Another way to deal with the problem is to give up the zero background constraint by allowing small fluctuations in the algorithm. This has not proved to be effective either. In Chapter Three, we are going to discuss the ice problem in detail.

Another obstacle in imaging frozen-hydrated yeast cells at our beamline is the coherence requirement. Theoretically, the diffraction pattern emerges from complete coherent illumination which is not possible in reality. For example, the x-ray beam at beamline 9.0.1 at the ALS has a coherence width of 8.7 μm. When the specimen is large compared to the coherence width of the beam, the coherence requirement will be unmet, which will lead to an un-reconstructable diffraction data. The freeze-dried cell shrinks considerably from pre-data-taking exposure: this is bad for several different reasons, but it actually appears to be an advantage as far as coherence requirements are concerned. Indeed, the cell we reconstructed in 2005 shrank significantly so that it met the coherence requirement to obtain a sensible reconstruction. On the other hand, for frozen-hydrated cells the coherence width of the beam appears to be not big enough to allow meaningful reconstructions. Over the past three years, we tried to reduce the cell size (by working with mutant cell lines) from 7 μm to about 2 μm to meet the coherence requirement on the sample

size. The detailed analysis of the coherence requirements and ways to deal with partial coherent illumination will be presented in Chapter Two.

When going from 2D imaging to 3D imaging, one of the very first steps is to assemble the 3D data cube. All the 2D diffraction patterns need to be put together with a common center. If some of these 2D patterns are not properly centered, meaning the centers of the some diffraction patterns are not the true zero spatial frequency position, the assembled 3D data will be distorted, and a reconstruction will be difficult to attempt. This centering problem also exists in 2D reconstructions. When the pattern is significantly shifted, a reconstruction may be very difficult. We developed a technique to find the real zero spatial frequency position. It has been tested with simulations and real data (the 2005 freeze-dried yeast cell data). We are going to discuss this method in Chapter Four.

Chapter 2

Coherence Properties of Photon Beam at BL 9.0.1 at the ALS

X-ray diffraction microscopy theoretically requires a fully coherent X-ray beam. When the coherence of the photon beam decreases, the quality of the speckles in the diffraction pattern degenerates. This may lead to a poorer reconstruction when the coherence is still relatively high, or it may make the reconstruction impossible when the coherence width (here and in the rest of the discussion, "width" refers to the standard one-sigma Gaussian rms width) is too small. It is controversial as to the exact coherence requirement for X-ray diffraction imaging. There is some discussion in the field [32], while no concrete conclusion has been reached.

The van Cittert-Zernike(VCZ) theorem is "traditionally" used in this type of calculation, which recently spurred debate on the validity of the theorem under the experimental conditions [33]. The VCZ theorem assumes the source to be incoherent, while the emittance-included photon beams from the un-

dulator can often be considered as partially coherent. The theorem [34] says that if the linear dimensions of the source and the distance between P_1 and P_2 are small compared to the distance of these points from the source,(the optics system is illustrated in Fig. 2.1) the complex degree of coherence μ_{12}

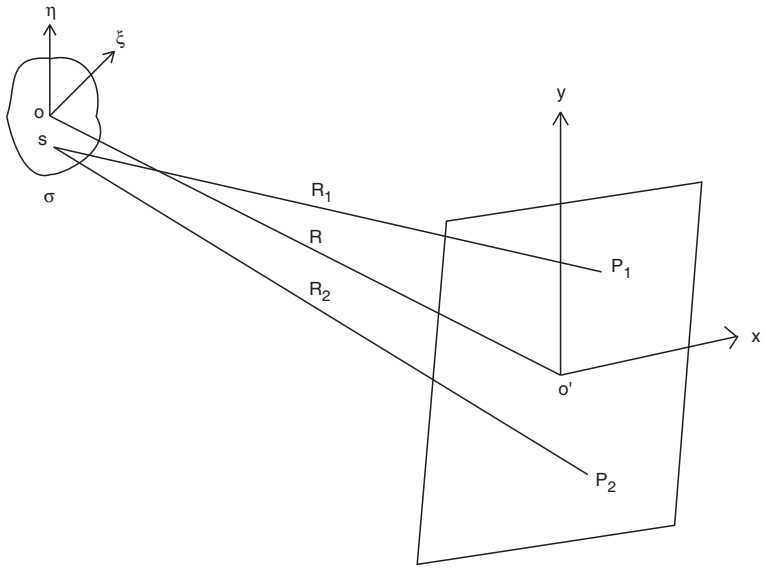

Figure 2.1: Illustration of the Van Cittert-Zernike theorem.

$$\mu_{12} = \frac{e^{\imath\psi} \iint_\sigma I(\xi,\eta) e^{\imath\overline{k}(p\xi+q\eta)} d\xi d\eta}{\iint_\sigma I(\xi,\eta) d\xi d\eta} \tag{2.1}$$

is equal to the normalized Fourier transform of the intensity function of the source, where $\overline{k} = \frac{2\pi}{\overline{\lambda}}$, $p = \frac{x_1 - x_2}{R}$, and $q = \frac{y_1 - y_2}{R}$. Here ψ represents the phase difference $\frac{2\pi(OP_1 - OP_2)}{\overline{\lambda}}$, which can be neglected when $OP_1 - OP_2 \ll \overline{\lambda}$.

In this chapter, we are going to perform an analytical calculation of the coherence width at the sample plane using the Gauss-Schell model [35], which assumes that all the waves and apertures are Gaussian. This is not an accurate description of the reality, but it is a good approximation which will give us the

right order of magnitude on the coherence width of the photon beam required for diffraction microscopy. One advantage of this approach is that, unlike the VCZ theorem, it doesn't have any constraints on the coherence of the source beam. In the end of the calculation, we will compare it with the VCZ theorem in various situations.

We are going to analyze the coherence properties of the emittance-included photon beam at BL 901 at the Advanced Light Source (ALS), Lawrence Berkeley National Laboratory (LBNL). Our goal is to first estimate the coherence width at the sample plane using the Gauss-Schell model, and then establish the coherence requirement for X-ray diffraction microscopy through simulations. Finally we are going to discuss about possible ways to deal with the partial coherence convolved into the diffraction data.

2.1 Theoretical Calculation of the Coherence Width at the Sample Plane

Before proceeding to the problem, we are going to define some symbols first: σ denotes the one-sigma Gaussian half-width; sub-indices x, y denote the properties in the horizontal and the vertical direction, respectively; sub-indices μ, I, and $\mathcal{M}$ represent the degree of coherence, the intensity and the mutual coherence function of the beam, respectively; and upper-indices s, zp, ph and sp refer to the beam at undulator source, zone plate, pinhole, and sample plane, respectively.

We will start with a simple situation, in which a Gaussian beam goes

through a lens for focusing. We will calculate the coherence width at far-field, and discuss the impact of the hard edge lens aperture on the coherence. A detailed analysis on the beam coherence at the BL 901 will then follow.

2.1.1 A Simple Example

Let's consider the following situation: a Gaussian source of width σ_I^s and coherence width σ_μ^s, that is imaged by a lens (or zone-plate, we will use "zp" to denote it) with focal length f and diameter D, whose source distance and image distance are S and S' respectively. What is the coherence width of the beam at the image position (which will be denoted as σ_μ^i, where i stands for "image position"), and at a distance z downstream from the image position (where z is in the far field, and will be denoted as the "sample plane")? For simplicity, we will discuss the beam properties in the x direction only and the sub-index x will be omitted in this example.

The width $\sigma_{\mathcal{M}}^s$ of the mutual coherence function at the source is given by [35, Eq. 16]

$$\frac{1}{(\sigma_{\mathcal{M}}^s)^2} = \frac{1}{(\sigma_\mu^s)^2} + \frac{1}{4(\sigma_I^s)^2}\,, \tag{2.2}$$

where σ_μ^s is the coherence width at the source and σ_I^s is the intensity width at the source.Then we can propagate the beam downstream for a distance S, to the lens position. The wave properties at this plane are given by [35]

$$\sigma_{\mathcal{M}}^{zp} = \sigma_{\mathcal{M}}^s \sqrt{1 + (\frac{S}{k\sigma_{\mathcal{M}}^s \sigma_I^s})^2} \tag{2.3}$$

$$\sigma_I^{zp} = \sigma_I^s \sqrt{1 + (\frac{S}{k\sigma_{\mathcal{M}}^s \sigma_I^s})^2}\,, \tag{2.4}$$

where k is the wave-number of the source. In other words, the ratio of coherence width to intensity width remains constant during free-space propagation. From the relationship

$$\frac{1}{(\sigma_{\mu}^{sp})^2} = \frac{1}{(\sigma_{\mathcal{M}}^{sp})^2} - \frac{1}{4(\sigma_{I}^{sp})^2}\,, \tag{2.5}$$

we can infer the coherence width, σ_{μ}^{zp}, at the lens position.

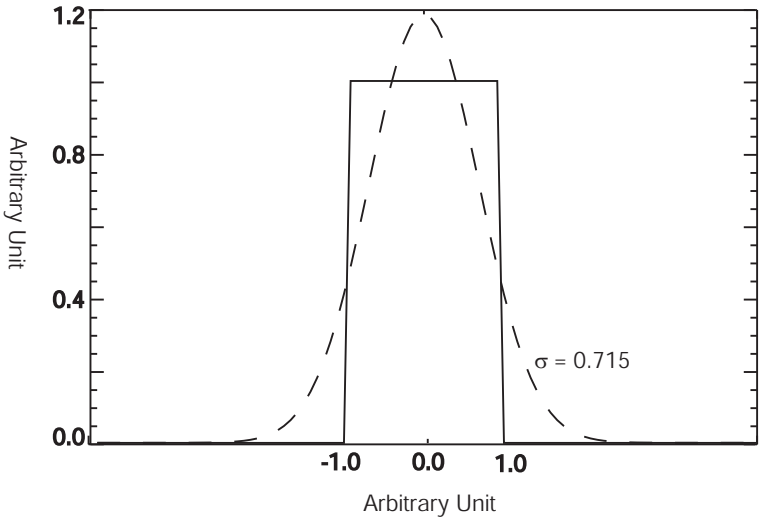

Figure 2.2: Using a Gauss function to fit a step function to approximate the Gaussian width of a hard edge lens aperture.

Since the lens (or zone plate) and all apertures in the experiment have hard edges, while the Gauss-Schell model assumes Gaussian functions throughout, we must find an appropriate Gaussian approximation of a hard-edged aperture. A least squares fit of a Gaussian function $Ae^{\frac{-x^2}{2\sigma^2}}$ onto a rectangle function with a height of 1 and a width of 2 yielded $A = 1.19$ and $\sigma = 0.715$, such that 89% of the area under the Gaussian is contained (see Fig. 2.2). This suggests that we could use $\sigma_{zp} = 0.358D$ to approximate the Gaussian half-width of the

lens with a diameter of D. If $\sigma_{zp} < \sigma_I^{zp}$, the beam size after the lens will be collimated to the aperture size; otherwise, it will remain the same. If we use $\sigma_I^{'zp}$ to refer to the beam size right after the lens, we have

$$\begin{cases} \sigma_I^{'zp} = \sigma_{zp} = 0.358D, \ \sigma_{zp} < \sigma_I^{zp}\,, \\ \sigma_I^{'zp} = \sigma_I^{zp} = \frac{\sigma_I^s \sigma_\mu^{zp}}{\sigma_\mu^s}, \ \text{otherwise}\,. \end{cases} \tag{2.6}$$

In the case that the aperture is collimating the beam, it is equivalent to having a source at the undulator with an effective coherence width $\sigma_\mu^{'s}$, which will entail $\sigma_I^{'zp}$. According to the properties of the Gauss-Schell model, this effective coherence width can be obtained as

$$\sigma_\mu^{'s} = \sigma_\mu^{zp} \frac{\sigma_I^s}{\sigma_I^{'zp}}\,. \tag{2.7}$$

Otherwise, nothing needs to be changed, and we will have $\sigma_\mu^{'s} = \sigma_\mu^s$.

By using the effective coherence width at the source as suggested by Eq. 2.7, we have taken into account the hard edge aperture impact on the coherence, so all the lens does now is demagnifying the source. The de-magnification is given by the ratio of the image and source distance of the lens, which is $M = S'/S$. Therefore, the beam width at image plane is

$$\sigma_I^i = M \cdot \sigma_I^s\,. \tag{2.8}$$

We can use the properties of the Gauss-Schell beams again to calculate the

coherence width at the image plane:

$$\sigma_{\mu}^{i} = \sigma_{\mu}^{'s} \frac{\sigma_{I}^{i}}{\sigma_{I}^{s}} \,. \tag{2.9}$$

We now have the coherence width and the beam intensity width at the image plane of the lens. In the following, we are going to calculate the coherence width of the beam in the far field, which is at a distance z downstream from the image position. We call this position the "sample plane," as in the X-ray diffraction microscopy experiment a sample would be placed here. The method used here is basically the same as when we tried to obtain the coherence width at the lens position.

The width of the mutual coherence function at the image position can be inferred from [35, Eq. 16]

$$\frac{1}{(\sigma_{\mathcal{M}}^{i})^2} = \frac{1}{(\sigma_{\mu}^{i})^2} + \frac{1}{4(\sigma_{I}^{i})^2} \,. \tag{2.10}$$

The wave properties at the sample plane follow

$$\sigma_{\mathcal{M}}^{sp} = \sigma_{\mathcal{M}}^{i} \sqrt{1 + (\frac{z}{k\sigma_{\mathcal{M}}^{i}\sigma_{I}^{i}})^2} \tag{2.11}$$

$$\sigma_{I}^{sp} = \sigma_{I}^{i} \sqrt{1 + (\frac{z}{k\sigma_{\mathcal{M}}^{i}\sigma_{I}^{i}})^2} \,, \tag{2.12}$$

where k is the wave-number of the X-ray beam. Finally the coherence width at the sample plane can be inferred from the relationship

$$\frac{1}{(\sigma_{\mu}^{sp})^2} = \frac{1}{(\sigma_{\mathcal{M}}^{sp})^2} - \frac{1}{4(\sigma_{I}^{sp})^2} \,. \tag{2.13}$$

2.1.2 Detailed Analysis on the Beam Coherence at the BL 901, ALS, LBNL

In this section, we are going to carry out a detailed analysis on the beam coherence at Beamline 9.0.1 at the ALS, LBNL. The beam is emitted from an undulator (U10), which consists of 43 periods with each period having a length of 0.10 m. The full length of the undulator is then 4.3 m. The beam at the undulator has a width of $\sigma_{Ix}^s = 310$ μm in the horizontal direction, and a width of $\sigma_{Iy}^s = 23$ μm in vertical. The coherence width at this point is given by the width of the single-electron radiation from an axially extended source of finite wavelength. It can be written as

$$\sigma_\mu^s = \frac{1}{4\pi}\sqrt{\lambda L}\,, \tag{2.14}$$

where σ_μ^s is the width of the coherence at source, λ is the wavelength and L is the length of the undulator [36]. The beam line is designed to work at the third undulator harmonic, which provides photon energies between 500 eV to 800 eV. For frozen-hydrated biological samples, the best contrast is obtained between the carbon and oxygen absorption edges at 290 and 540 eV, respectively, so a photon energy of 520 eV (wavelength $\lambda = 2.38$ nm) was used in many of our experiments. Thus, the coherence width of the beam is given by

$$\sigma_\mu^s = \frac{1}{4\pi}\sqrt{2.38 \text{ nm} \cdot 4.3 \text{ m}} = 8.06 \ \mu\text{m}\,. \tag{2.15}$$

A schematic (not to scale) of the beamline is shown in Fig. 2.3. The beam from the undulator first impinges on a Ni mirror, which focuses the beam

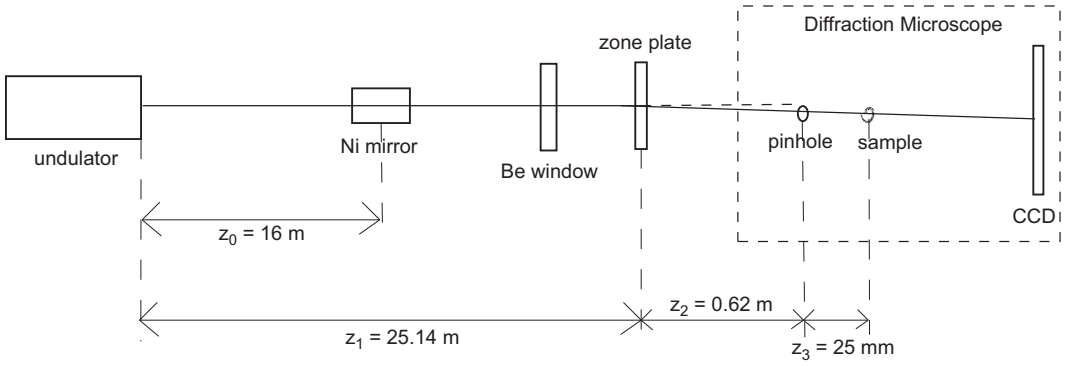

Figure 2.3: The schematics of beamline 9.0.1 at the ALS, Berkeley. Not shown to actual scale.

in horizontal direction. We have a Be window downstream of the Ni mirror. Then an off-axis zone plate is used as a monochromator [37]; it splits the beam of different wavelengths onto different focal points. A pinhole is placed downstream of the zone plate at a distance equal to its focal distance of the given wavelength, to pick up the right energy beam from the rainbow spectrum at that plane. This pinhole redefines the beam size and the coherence of the beam. The Airy pattern of the pinhole creates a bright spot on the sample, and its diffraction pattern is collected by a CCD camera at the end of the beamline.

The Ni mirror, located at 16 m downstream from the undulator, deflects the photon beam to BL 901 with an incident angle of 3°. This Ni mirror focuses the beam horizontally with the focus at 16 m downstream of the mirror [38]. This will only affect the horizontal beam size at the zone plate plane, which is now identical to the size of beam at $z_1' = 2z_0 - z_1 = 6.86$ m from the undulator given the symmetry of the optics. Following the Gauss-Schell model, we have

the horizontal and vertical beam width at zone plate to be

$$\sigma_{Ix}^{zp} = 350\ \mu\mathrm{m}\,, \tag{2.16}$$

$$\sigma_{Iy}^{zp} = 1.20\ \mathrm{mm}\,. \tag{2.17}$$

The Be window has an aperture much larger than the beam size; from the last section, we know that it will not modify the coherence properties of the beam. The element downstream of Be window is the zone-plate. The beam size at that plane (obtained by using the Gauss-Schell model) can be used to calculate the divergence of the photon beam caused by single electron radiation. It can be written explicitly as

$$\sigma'_{x\phi} = \frac{\sigma_{Ix}^{zp} - \sigma_{Ix}^{s}}{z_1} = 1.58\ \mu\mathrm{rad} \tag{2.18}$$

$$\sigma'_{y\psi} = \frac{\sigma_{Iy}^{zp} - \sigma_{Iy}^{s}}{z_1} = 46.9\ \mu\mathrm{rad}\,. \tag{2.19}$$

The ALS storage ring parameters [39] show that the divergence of the beam at our source is

$$\sigma'_{xr} = 23\ \mu\mathrm{rad} \tag{2.20}$$

$$\sigma'_{yr} = 6.5\ \mu\mathrm{rad}\,, \tag{2.21}$$

in the horizontal and vertical directions respectively. The total divergence of

the beam can then be obtained as [36, Eq. 30]

$$\sigma'_x = \sqrt{(\sigma'_{xr})^2 + (\sigma'_{x\phi})^2} = 23.0\ \mu\text{rad} \tag{2.22}$$

$$\sigma'_y = \sqrt{(\sigma'_{yr})^2 + (\sigma'_{y\psi})^2} = 47.3\ \mu\text{rad}\,. \tag{2.23}$$

Thus the beam size at the zone-plate, after taking the divergence of the beam into account, is

$$\sigma^{zp}_{Ix} = \sigma^{s}_{Ix} + \sigma'_x \cdot z_1 = 889\ \mu\text{m} \tag{2.24}$$

$$\sigma^{zp}_{Iy} = \sigma^{s}_{Iy} + \sigma'_y \cdot z_1 = 1.21\ \text{mm}\,. \tag{2.25}$$

Now we are ready to apply the Gauss-Schell model to obtain the coherence width at the zone-plate plane:

$$\sigma^{zp}_{\mu x} = \frac{\sigma^{zp}_{Ix}\sigma^{s}_{\mu x}}{\sigma^{s}_{Ix}} = 23.1\ \mu\text{m} \tag{2.26}$$

$$\sigma^{zp}_{\mu y} = \frac{\sigma^{zp}_{Iy}\sigma^{s}_{\mu y}}{\sigma^{s}_{Iy}} = 412\ \mu\text{m}\,. \tag{2.27}$$

The diameter of the zone-plate is 500 μm. As discussed in the last section, the Gaussian width of the zone-plate can be approximated through a Gaussian fit as 179 μm. Therefore, the beam with at the zone-plate (σ^{zp}_{Ix} and σ^{zp}_{Iy}) is much bigger than the zone-plate width, in which case the beam after the zone-plate will be restricted by the lens aperture. Following the calculation in the last section, we have an effective coherence width of

$$\sigma^{'s}_{\mu} = 53.1\ \mu\text{m}\,. \tag{2.28}$$

Similar to a lens, the demagnification of the zone-plate is given by its source and image distance. In our system, $M = z_2/z_1 = 0.025$. It follows that the beam widths at the pinhole are

$$\sigma_{Ix}^{ph} = M \cdot \sigma_{Ix}^{s} = 7.7\ \mu\text{m} \tag{2.29}$$

$$\sigma_{Iy}^{ph} = M \cdot \sigma_{Iy}^{s} = 0.57\ \mu\text{m}\,, \tag{2.30}$$

and the coherence width at the pinhole are

$$\sigma_{\mu x}^{ph} = \sigma_{\mu y}^{ph} = \frac{\sigma_{\mu}^{'s}\sigma_{Ix}^{ph}}{\sigma_{Ix}^{s}} = 1.3\ \mu\text{m}\,. \tag{2.31}$$

Given the diameter of the pinhole is 5.5 μm corresponding to a best Gauss fit with σ of 1.97 μm, the beam width after the pinhole will again be restricted to the pinhole width.

Next, we propagate the beam from the pinhole to the far-field sample plane, just as what we did in the last section, and we have the beam width and coherence width at the sample plane to be

$$\sigma_{Ix}^{sp} = 7.9\ \mu\text{m} \tag{2.32}$$

$$\sigma_{Iy}^{sp} = 11.1\ \mu\text{m} \tag{2.33}$$

$$\sigma_{\mu x}^{sp} = 5.3\ \mu\text{m} \tag{2.34}$$

$$\sigma_{\mu y}^{sp} = 25.3\ \mu\text{m}\,. \tag{2.35}$$

Before move on to the next topic, let's take a moment to discuss the validity of the VCZ theorem. The Gauss-Schell model entails a vertical beam width

of 1.20 mm at the zone-plate plane, which results in a coherence width of 412 μm at that plane. The vertical width of the photon source (23 μm) is larger than its coherence width (8.06 μm). Can we then consider the source to be incoherent and apply the VCZ theorem to get the coherence width at the zone-plate?

As the theorem stated, the complex degree of coherence at zone-plate is given by the Fourier transform of the intensity distribution at the undulator source, which in our case is Gaussian. So the complex degree of coherence will also have a Gaussian distribution, with widths

$$\sigma_{\mu y}^{zp} = \frac{\lambda z_1}{2\pi\sigma_{Iy}^{s}} = 415\ \mu\mathrm{m}\,. \tag{2.36}$$

Comparing to what we get from the Gauss-Schell model, the difference is only 0.7%, which is within the tolerance of our model and measurements.

However, if we look at the coherence width at the sample plane, from the results at the pinhole, the VCZ theorem will suggest a vertical coherence width of 7.6 μm at the sample. This is very different from the result of the Gauss-Schell model, 25.3 μm. It is not difficult to see that the reason that the VCZ theorem is invalid here is that the beam size at the pinhole is even smaller than the coherence width in the vertical direction. In this case, the beam may be regarded as coherent rather than incoherent.

Therefore, when using VCZ theorem in the calculation, we need to take into account the incoherent source requirement. It cannot be applied when the beam width is comparable to the coherence width.

2.2 Simulations

As we see in last section, the coherence width at the sample plane, especially in the horizontal direction (5.3 μm), is actually quite close to the size of the samples (2-7 μm in diameter) used in our experiment. To illustrate the effect of the partial coherence on the data and consequently on the reconstruction, in this section we are going to present a simulation of the experiment with partially coherent illumination.

2.2.1 Build a Cell

First, we built a fake cell in an ice cube. The dimension of the cube is $512 \times 512 \times 512$ pixels, the diameter of the fake cell is 100 pixels, and the voxel size is $(2\text{ nm})^3$. The membrane of the cell is made by lipid. The cell is filled with soluble protein and has one ellipsoid protein bulk and two protein cylinders inside. Suppose the x-ray beam illuminates along the z axis. The center of the cell was located on the exit plane of the ice cube along the z axis, which is set to be the focal plane, and the protein structures were cut off by this focal plane. Thus, only half of the cell remains in the cube. The Henke data [40] are used for the phase and attenuation response of protein, ice and lipid. The simulation is done by IDL routine "tomo_buildcell.pro", written by C. Jacobsen, and modified by H. Miao.

To simulate the exit wave on the focal plane, the multi-slice propagation method was used, in which the ice cube is cut into a series of thin slices perpendicular to z axis; the diffraction pattern after each slice is propagated to the one behind it. This is done by IDL routine "tomo_multiprop.pro"

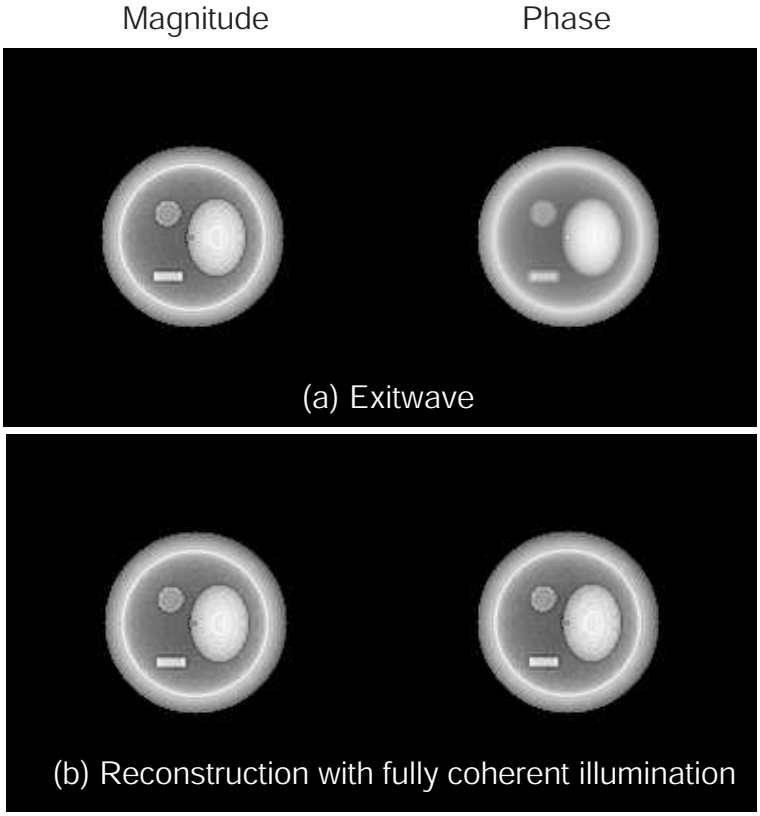

Figure 2.4: (a) Exit wave of the fake cell consisting of lipid membrane, soluble protein and protein bulks inside the cell; (b) the reconstruction of the diffraction pattern with fully coherent illumination obtained by using difference map method.

by C. Jacobsen. In the simulations, the exit wave is generated with 10000 incident photons per pixel, done in IDL routine "diff_noise.pro" by H. Miao, in which routine "add_photon_noise.pro," created by C. Jacobsen, modified by H. Miao, is called to add photon noise and CCD's dark current to obtain the final diffraction pattern.

Fig. 2.4 shows both the magnitude and phase of the exit wave and the reconstruction of the diffraction pattern with fully coherent illumination. The reconstruction has been done by using the difference map method as was discussed in Chap. 1.[24].

2.2.2 With Partial Coherent Illumination

We then generated the diffraction pattern when the illumination is not fully coherent. According to the Schell theorem if we have a partially coherent beam with complex degree of coherence $\mu(\Delta x, \Delta y)$, incident on a sample, which is described by some pupil function whose autocorrelation is $P(\Delta x, \Delta y)$, the diffraction intensity $I(k_x, k_y)$ can be obtained as

$$I(k_x, k_y) = \frac{I_0}{\overline{\lambda z}} \iint P(\Delta x, \Delta y)\mu(\Delta x, \Delta y)e^{\imath\frac{2\pi}{\lambda z}(k_x\Delta x + k_y\Delta y)}d\Delta x d\Delta y \qquad (2.37)$$

Therefore, the diffraction intensities are given by a Fourier transform on the autocorrelation of the pupil function multiplied by the complex degree of coherence. The autocorrelation of the pupil function is obtained by performing a Fourier transform on the pupil function, taking the intensity of it, and then applying an inverse Fourier transform. The complex degree of coherence can be regarded as a real Gaussian function here [41]. Since in the simulation, the

cell has a diameter of 0.2 μm, we generated diffraction patterns with coherence widths of 0.2 μm, 0.4 μm, 0.8 μm, 1.6 μm, and 5.0 μm. Fig. 2.5 shows the diffraction pattern with full coherence (left) and with coherence widths of 0.2 μm (right). An enlarged image of a small segment is shown on the top of each image which shows the detailed speckles. As expected, the speckles from a partial coherent illumination are blurred compared to the ones from fully coherent illumination. Now, we would like to see how well these patterns can be reconstructed.

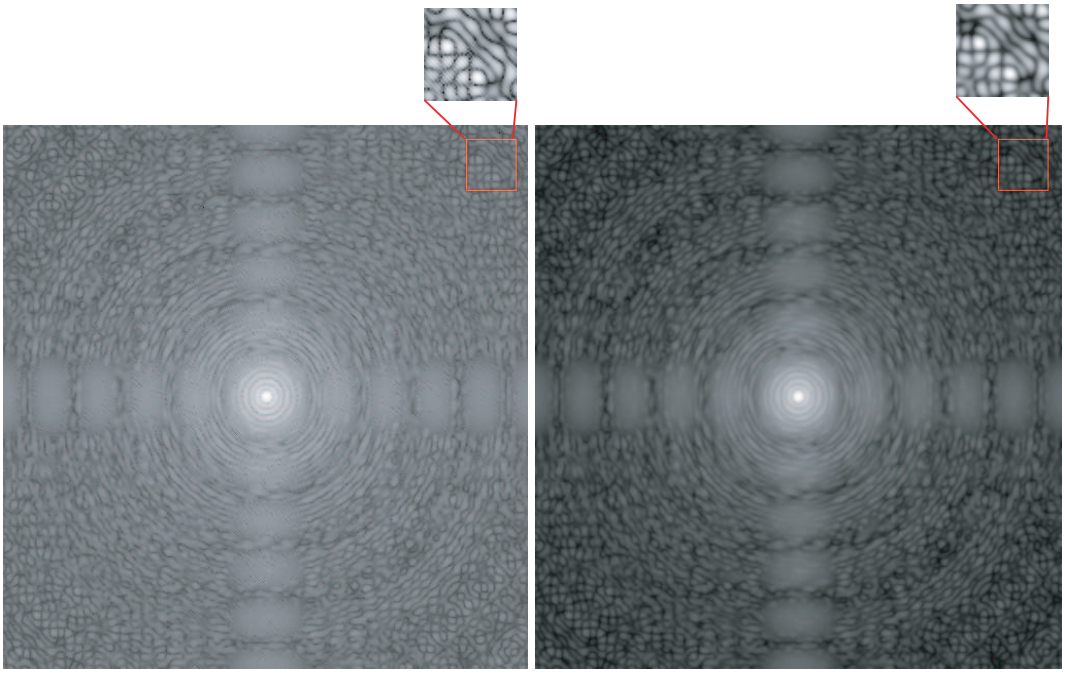

Figure 2.5: Left: diffraction pattern of a simulated cell-like protein object with a diameter of 0.2 μm with fully coherent illumination; right: diffraction pattern of the same simulated cell with partial coherent illumination (coherence width = 0.2 μm). An enlarge image of a small segment is shown on the top of each pattern in which detailed speckles can be observed. As coherence is worsened, the speckles get "fuzzy".

Fig. 2.6 shows the reconstructions of the cell with illumination of different

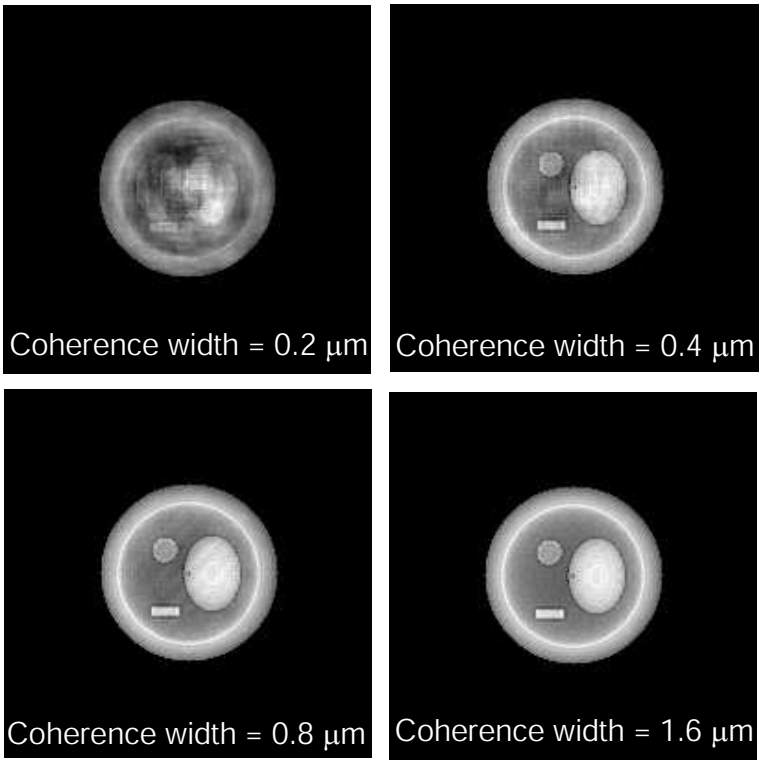

Figure 2.6: Retrieved magnitudes of the diffraction patterns from illumination with different coherence widths of the simulated cell with a diameter of 0.2 μm. Retrieved phases present a similar behavior.

coherence widths. Clearly, the quality of the reconstruction is poor as the coherence width equals to the cell size. When the coherence width is twice as big as the cell size, a reasonable reconstruction can be obtained. When the coherence width is more than three times the cell size, there are no apparent artifacts in the reconstruction.

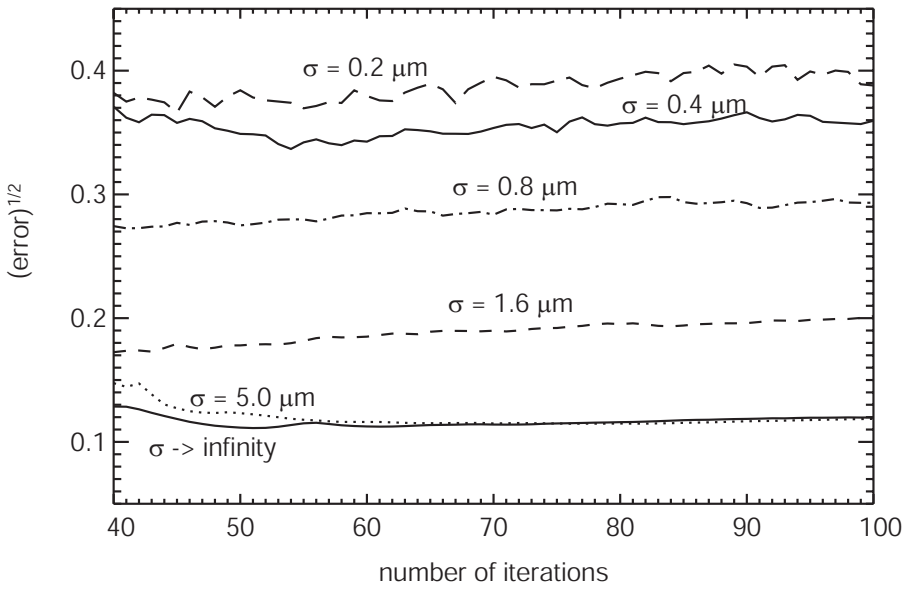

Figure 2.7: Plot of square-root of the errors of the 40th to the 100th iteration with different coherence widths (σ's).

Fig. 2.7 plots the errors of the 40th to the 100th iteration with different coherence widths. To show the differences more clearly, we plot the square-root of the errors. The convergence of the algorithm becomes worse when the coherence width becomes smaller. When the coherence width is at least 25 times the sample size, it can be considered as fully coherent. The coherence of the illumination has an significant impact on the quality of the reconstruction.

Given the coherence width at sample plane of this beamline, the cells be

imaged should be no bigger than 3 μm with the present geometry of wavelength (2.4 nm corresponding to 512 eV), pinhole diameter (5.5 μm) and pinhole-to-sample distance (25 mm).

2.2.3 De-convolve the Partial Coherence

As the simulation shows, the degree of coherence has been convolved into the diffraction pattern. It sets the upper limit of the cell size that could be reconstructed with given coherence width. In general, we require the coherence width to be at least 4 times the radius of the cell. However, if we can obtain the function of the degree of coherence in experiment, it is possible to de-convolve it from the data so that the influence of the partial coherence can be largely mitigated. As we see in Fig. 2.6, when the coherence width is 0.2 μm, the cell whose radius is 0.1 μm can't be reconstructed. Since the degree of coherence is known in the simulation (which is a Gaussian function), we can then try to de-convolve it from the diffraction data.

The autocorrelation of data can be obtained by performing an inverse Fourier transform of the intensity data. In real space, all we need to do is to divide the autocorrelation by the degree of coherence function to get a new autocorrelation. The estimated correct data is the intensity of the Fourier Transform of the new autocorrelation.

There are several things to be careful about in this procedure. First, at the edge of the image, the autocorrelation signal tends to be low and the magnitude of the degree of coherence is low too. This could cause problems when doing division or Fourier transform. To eliminate this "edge problem,"

we apply a mask when doing the division. The mask allows the action only being performed at the relative center of the image; in our case the mask filters out the pixels where the degree of coherence is less than 0.2. Second, in reality, this degree of coherence has to be measured in experiment. Often times, there could be zeros in the function. To avoid the problem of overflow due to "dividing by zero," we can add a small ϵ to the degree of coherence $\mu(x, y)$ before doing the division. So the modified autocorrelation $R'(x, y)$ with the degree of coherence being de-convolved can be obtained as

$$R'(x, y) = \frac{R(x, y)}{\mu(x, y) + \epsilon}, \tag{2.38}$$

where $R(x, y)$ is the autocorrelation of the original data. The value of ϵ is related to the photon noise in the measure of degree of coherence, hence related to the incident photon number in the experiment.

In simulations, this procedure works beautifully. One example is shown in Fig. 2.8. The left image is the reconstruction of the cell with partial coherent illumination (coherence width = 0.2 μm); and the right one is the reconstruction after de-convolving the degree of the coherence. We can see little impact of the partial coherence in the right one. However, in experiment, it could be challenging to determine the degree of coherence accurately.

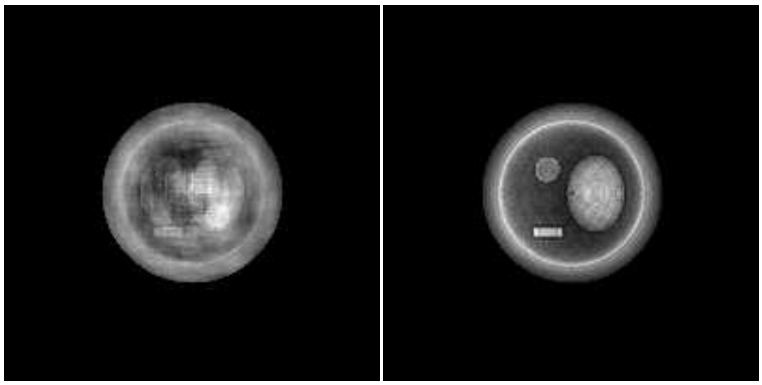

Figure 2.8: Retrieved magnitudes of the diffraction patterns with coherence width = 0.2 μm before (left) and after (right) applying the de-convolution method.

2.3 Coherence Data from BL 9.0.1 and the Analysis

In this section we are going to look at the data from a classic double-pinhole diffraction experiment, which is an extension of Young's two-slit interference experiment. We would like to extract the degree of coherence from the diffraction pattern of the pinholes with different separations.

2.3.1 Data Analysis

Consider the far-field diffraction pattern of two illuminated pinholes. If there is no mutual coherence between the illumination on one pinhole and the illumination on the other, one will obtain the overlap of two pinhole diffraction patterns (that is, a single aperture Airy diffraction pattern with twice the intensity). If however there is perfect mutual coherence between the illumination function on the two pinholes, one will obtain a single aperture Airy diffraction

pattern with a fringe pattern superimposed on it. If one were to use the two different illumination patterns as a transparency function to be illuminated by a laser, in the fully incoherent case one would produce in the far field a centrally symmetric illumination pattern characteristic for the Fourier transform of an Airy pattern. In the fully coherent case, the interference fringes would redistribute part of the light to first order diffraction peaks (each with the shape of the Fourier transform of the Airy pattern) on either side of the optical axis. By measuring the fraction of energy contained in the diffracted patterns versus the central one (as shown in Fig. 2.9), one can obtain a measure of the degree of coherence in the original illumination [42].

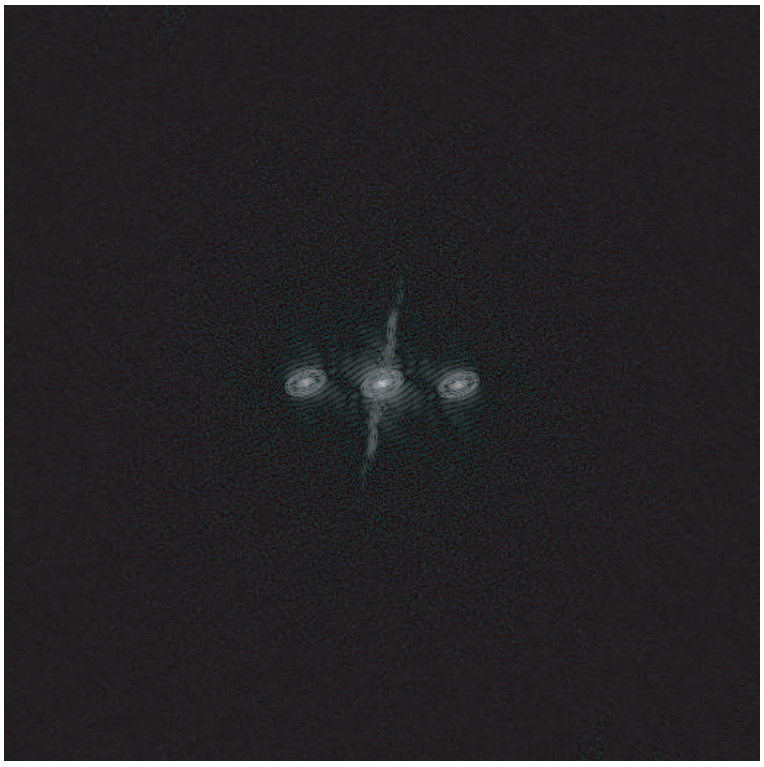

Figure 2.9: The autocorrelation of an x-ray diffraction data of a pinhole pair with 2 micron separation.

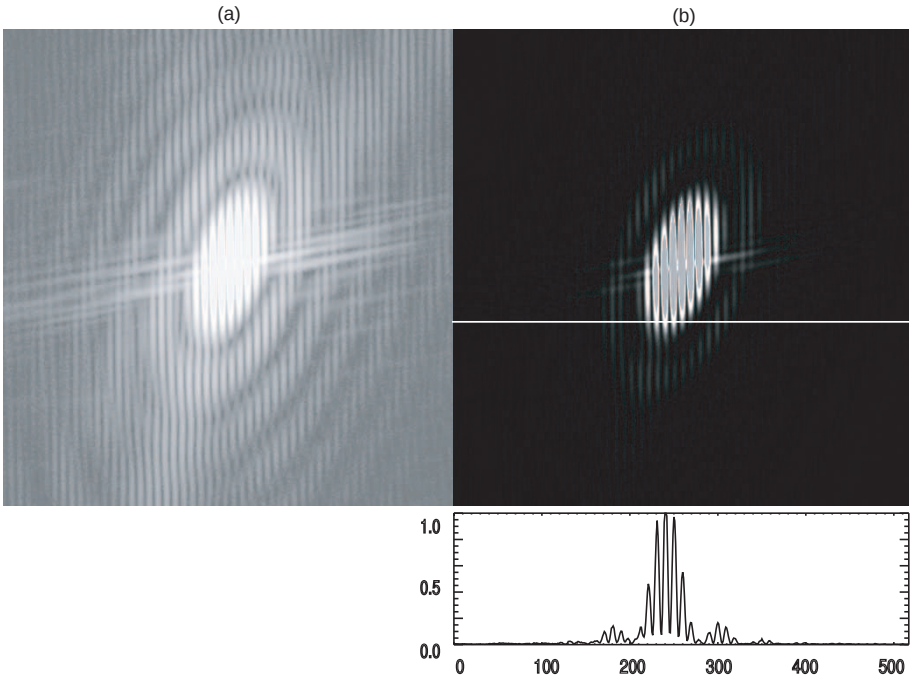

Figure 2.10: X-ray diffraction pattern of a pinhole pair with 2 micron separation with a scan line across the image: (a) in log-log scale; (b) in linear scale. Note that the center part of the data is saturated due to the high flux of the beam, so we chose to scan in an area that contains no saturation. Its autocorrelation is shown in Fig. 2.9.

Fig. 2.10 shows the diffraction data whose autocorrelation has been shown in Fig. 2.9. From the data, we can clearly see the fringes. A horizontal scan line across the data is shown at the bottom of (b). By reading the maxima and the adjacent minima, we estimate the visibility or contrast to be about $(86 \pm 4)\%$. A more accurate measure requires utilizing as many data points as possible. However, the Airy spot indicates that the holes are not really circular, and it's tilted in the x-y plane. This irregularity of the pinhole shape makes a good fit to the data very difficult. One alternative would be calculating the degree of coherence from the autocorrelation, as mentioned above.

For a pair of pinholes, displaced by x_0 from each other, the autocorrelation can be obtained as following (for simplicity, here we ignore the phase of the complex degree of coherence, β_{12}, which should be a very small value close to zero):

$$
\begin{aligned}
D(x) &= \int 2I^{(0)}(k)(1 + |\mu_{12}| \cos kx_0) e^{2\pi\imath kx} dk && (2.39)\\
&= \int 2I^{(0)}(k) e^{2\pi\imath kx} dk + \frac{|\mu_{12}|}{2} \int 2I^{(0)} e^{2\pi\imath k(x - \frac{x_0}{2})} dk && (2.40)\\
&\quad + \frac{|\mu_{12}|}{2} \int 2I^{(0)} e^{2\pi\imath k(x + \frac{x_0}{2})} dk && (2.41)\\
&= I_C + I_L + I_R \,, && (2.42)
\end{aligned}
$$

where $D(x)$ is the autocorrelation function, $I_C = \int 2I^{(0)} e^{2\pi\imath kx} dk$ denotes the center spot in the pattern, $I_L = \frac{|\mu_{12}|}{2} \int 2I^{(0)} e^{2\pi\imath k(x - \frac{x_0}{2})} dk$
and $I_R = \frac{|\mu_{12}|}{2} \int 2I^{(0)} e^{2\pi\imath k(x + \frac{x_0}{2})} dk$ are corresponding to the left spot and the right spot, respectively.

Now, if we look at the norm of I_C, we have

$$\int |I_C|^2 dx = \int dx \iint I_0(k) I_0^*(k') e^{2\pi\imath(k-k')x} dk dk' \tag{2.43}$$

$$= \iint I_0(k) I_0^*(k') \delta(k-k') dk dk' \tag{2.44}$$

$$= \int |I_0(k)|^2 dk \,. \tag{2.45}$$

Similarly, we have

$$\int |I_L|^2 dx = \frac{|\mu_{12}|^2}{4} \int |I_0(k)|^2 dk \tag{2.46}$$

$$\int |I_R|^2 dx = \frac{|\mu_{12}|^2}{4} \int |I_0(k)|^2 dk \,. \tag{2.47}$$

So, the degree of coherence $|\mu_{12}|$ can be obtained as

$$|\mu_{12}| = \sqrt{2 \frac{\int |I_L|^2 dx + \int |I_R|^2 dx}{\int |I_C|^2 dx}} \,. \tag{2.48}$$

This is illustrated in Fig. 2.9, where there are three bright spots in the autocorrelation. The central one corresponds to the main profile of the Airy pattern, while the two side spots result from the fringes. Fig. 2.11 shows the results of the Fourier transform on the central spot only, or on the two side spots only.

The results are summarized in Table 2.1. The first column is the separation of the two pinholes, the second column gives the names of the data files used, and the third column is the $|\mu_{12}|$ obtained by using Eq. 2.48. Fig. 2.12 shows the plot of the degree of coherence in both the x and the y directions. At one-sigma half width of a Gaussian distribution, the magnitude drops to about

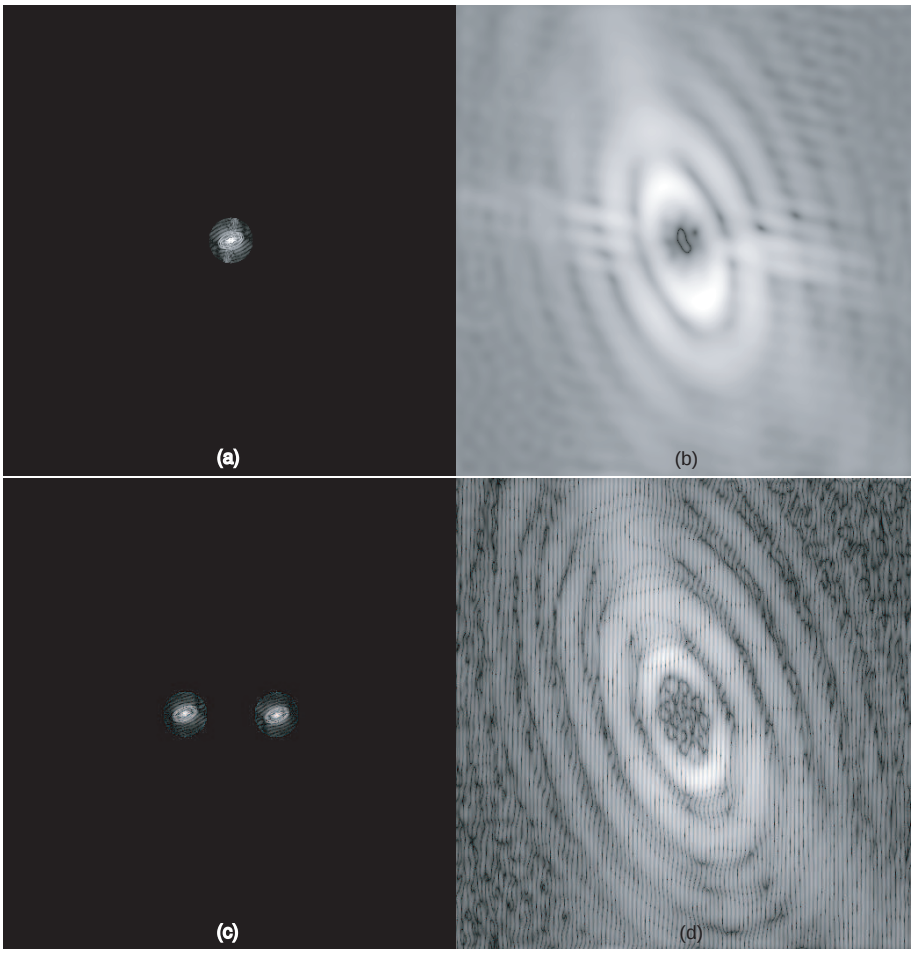

Figure 2.11: (a) the central spot of the autocorrelation; (b) the Fourier transform of (a); (c) the side spots of the autocorrelation; (d) the Fourier transform of (c).

x_0 (μm)	data file	$\lvert\mu_{12}\rvert$
2.10	dt_2007_09_13_0466.nc	0.897
2.06	dt_2007_09_13_0493.nc	0.872
2.04	dt_2007_09_13_0545.nc	0.866
5.12	dt_2007_09_13_0672.nc	0.682
5.12	dt_2007_09_13_0724.nc	0.665
5.14	dt_2007_09_13_0801.nc	0.665
8.46	dt_2007_09_13_0828.nc	0.321
9.36	dt_2007_09_13_0856.nc	0.200
9.44	dt_2007_09_13_0936.nc	0.167

Table 2.1: Results from the coherence experiments. The degree of mutual coherence $|\mu_{12}|$ was determined for different pinhole separations x_0 in experiments carried out at 750 eV at ALS beamline 9.0.1.

60%. In Fig. 2.12 we see that at 6 μm pinhole separation, the degree of coherence drops to 59%. Therefore, from the coherence experiment we estimate the coherence width at the sample plane to be around 6 μm.

2.3.2 Discussion

We see an obvious decrease in degree of coherence as the separation of the pinholes increases. However, the data suggests a coherence width around 6 μm in both the horizontal and the vertical directions. The horizontal width is in agreement with our theoretical prediction, which is 5.3 ± 1.1 μm. The 20% uncertainty is estimated from the tolerance in beamline measurements and imperfection of the optics. But the vertical coherence width is much smaller than what we thought, which is 25.3 μm. This can be explained by the "forgiveness factor" [43], where one has reduced sensitivity to mirror surface imperfections in the horizontal direction in the case of vertical grazing angle reflection, and vice versa. As there are imperfection on the Ni mirror surface,

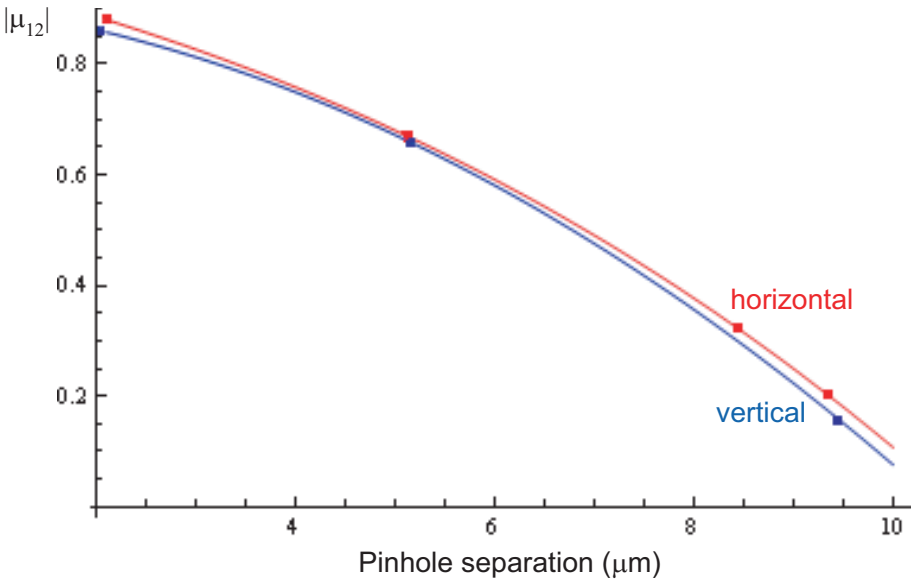

Figure 2.12: Plot of the degree of coherence in both the x and the y directions. The interpolation curves are smooth lines through the data points. The degree of mutual coherence $|\mu_{12}|$ was determined for different pinhole separations x_0 in experiments carried out at 750 eV at ALS beamline 9.0.1.

and the mirror is positioned to have a 3° incident angle, the horizontal optical tolerances are much bigger than the vertical ones. The horizontal beam size after the mirror could be achieved as the prediction in the calculation, while the vertical beam size might be much bigger than what we have computed. This difference in the beam size could grant the difference of the coherence width at sample plane in the vertical direction.

2.4 Summary

In this chapter, using the Gauss-Schell model, we calculated the coherence width at the sample plane for BL 9.0.1 at the ALS, LBNL. We discussed the validity of the VCZ theorem, and indicated the Gauss-Schell model as a substitute when the requirements for using VCZ theorem is unmet. Simulations were done to test the coherence requirements for X-ray diffraction microscopy. De-convolution method was provided to deal with data contaminated by partial coherence. Coherence data from BL 9.0.1 at the ALS were analyzed and compared with the theoretical calculation. While the results in the x direction agree with each other very well, the results in the y direction were not quite the same which can, however, be explained by the "forgiveness factor."

Chapter 3

Frozen-hydrated Sample Preparation and Analysis on Ice Background

After the successful reconstruction of the freeze-dried yeast cell [20], the group effort has been focused on experimenting with frozen-hydrated cells as they have a much closer status to living cells and thus could provide us more valuable structural information. However, there appear to be some tough issues in imaging frozen-hydrated cells. After two years of struggle, we have found that the ice accumulation is a major difficulty to overcome. Since the structure of the ice is different from point to point on the sample grid, its scattering pattern at the area where "no_sample" data is taken cannot be exploited to estimate the ice structure around the sample. It is not possible to subtract the ice background directly from the data. Since the scattering from the ice sometimes can be relatively strong, (unlike when dealing with dry

sample) we cannot assume an "empty" area around the cell which is required for a tight support constraint in the reconstruction procedure. Eliminating the ice background has been a daunting task in the experiments with frozen-hydrated cells.

If we examine the experimental procedure carefully, we would notice that the ice background forms mainly through three different stages of the experiment. It first occurs during plunging, then at sample transfer, and finally, as we discovered recently, also during the data collection inside the vacuum chamber. In this chapter, we will discuss how each step affects the ice accumulation on the grids and how to possibly avoid ice formation.

3.1 Why Frozen Hydrated?

As we mentioned before, frozen-hydrated samples preserve the instantaneous state of the cells in their natural environment. The structural information revealed by the imaging of a frozen-hydrated sample is of more biological virtue than that of a dried cell. This is the main reason of our move to image frozen-hydrated cells.

Another important virtue working at liquid nitrogen temperature when viewing frozen-hydrated cells is a dramatic reduction in sensitivity to radiation damage [44]. Frozen-hydrated cells are radiation-hard, and thus can bear much more dose than dried cells. Radiation damage comes from two aspects: direct damage to the molecules, and secondary chemical degradation by free radicals. While both occur in dried cells, the ice matrix of frozen-hydrated cells efficiently prevents the diffusion of free radicals. This protects the sample from

further damage of bond scission and mass loss. In Shapiro's Ph.D. research, he proved that frozen-hydrated yeast cells are much more stable than freeze-dried ones, since freeze-dried cells shrink significantly once in the beam [45]. Because high resolution imaging requires a large radiation exposure, a great tolerance of radiation will play an important role in this type of imaging.

Finally, imaging in the "water window" gives excellent natural contrast between ice and organelles. Water window refers to the radiation energy between 284 eV to 544 eV, within which the absorption of water and carbon presents a big difference which eliminates the needs for chemical staining. Fig. 3.1 illustrates the penetration distance in water and proteins for x-rays and electrons [46]. Here λ is the mean free path, $1/\mu$ is the $1/e$ attenuation length for x-rays.

For all these reasons, frozen-hydrated cells became our next candidate for imaging.

3.2 Plunge Frozen Hydrated Cells

Frozen-hydrated sample preparation was pioneered in cryo-electron microscopy (EM) in 1970's and 1980's [44]. The difficulty in such sample preparation is that when water freezes under normal condition, it forms a crystalline structure. Ice crystals may cause strong scattering in the diffraction pattern, hence interfering with the diffraction data from the sample. However, when freezing so rapidly that water molecules do not have the time to rearrange themselves into a crystal lattice, water can form a uniform layer of vitreous ice. Obviously, the key to get vitreous ice layer is to cool the water rapidly; this means at a cooling rate around 10,000 K/sec, which can be achieved by

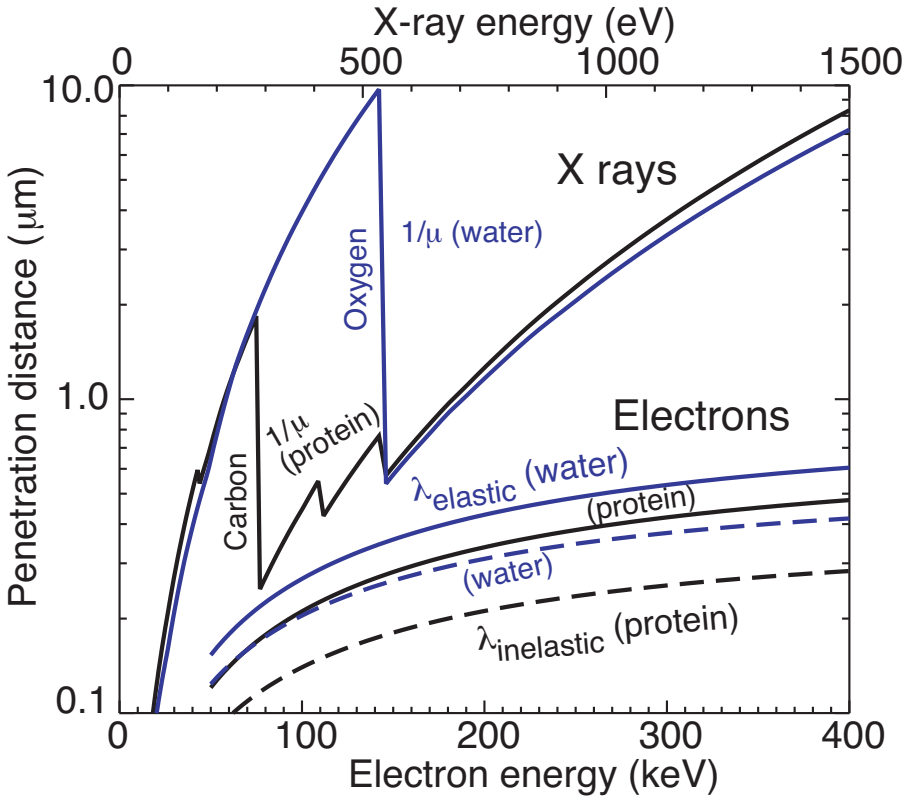

Figure 3.1: Penetration distance in water and proteins for x-rays and electrons. λ is the mean free path, $1/\mu$ is the $1/e$ attenuation length for x-rays [46].

plunging the sample quickly into liquid ethane. After the sample is frozen, it can be transferred from liquid ethane to liquid nitrogen for storage.

While this technique is pretty mature in cryo-EM, it is still challenging in x-ray microscopy since our samples are much thicker. In EM, because of the low penetrating power of electrons, typically the samples are less than 0.5 μm thick. However, in x-ray microscopy, we are imaging whole cells, which often have a size of 2 to 5 μm. To ensure that the whole cell can be cooled rapidly enough we first plunge the sample quickly into liquid ethane. After the sample is frozen, it is then transferred from liquid ethane to liquid nitrogen to avoid ice formation. The frozen sample is stored in a liquid nitrogen dewar.

This plunging process used to be done with "home-made" devices which inevitably introduce a great deal of vibration when plunging. It is also difficult to control the plunging speed, blotting parameters and cell environment, such as temperature and humidity. In 2006, we moved to using a Vitrobot, an automated plunge-freezing robot for aqueous suspensions developed by the FEI company. Fig. 3.2 is a picture of the system with Ken Downing (left), Bjorg Larson (center), and Andrew Stewart (right). This robot basically freezes the sample automatically within a closed space. One can easily change the environmental settings, blotting time, blotting offset, waiting time, etc. It plunges quickly and gently, bearing a high-yield of sample output.

In our preparation, we first dilute the cell suspension to a desired concentration. This usually means around 15 cells per square on the cellometer, see Fig. 3.3. Then with a pipette, we drop 5 μl cell solution onto a copper based formvar coated grid. Fig. 3.4 shows a visible light microscope image of a typical coated grid with cells on it. We lay the grid horizontally on the

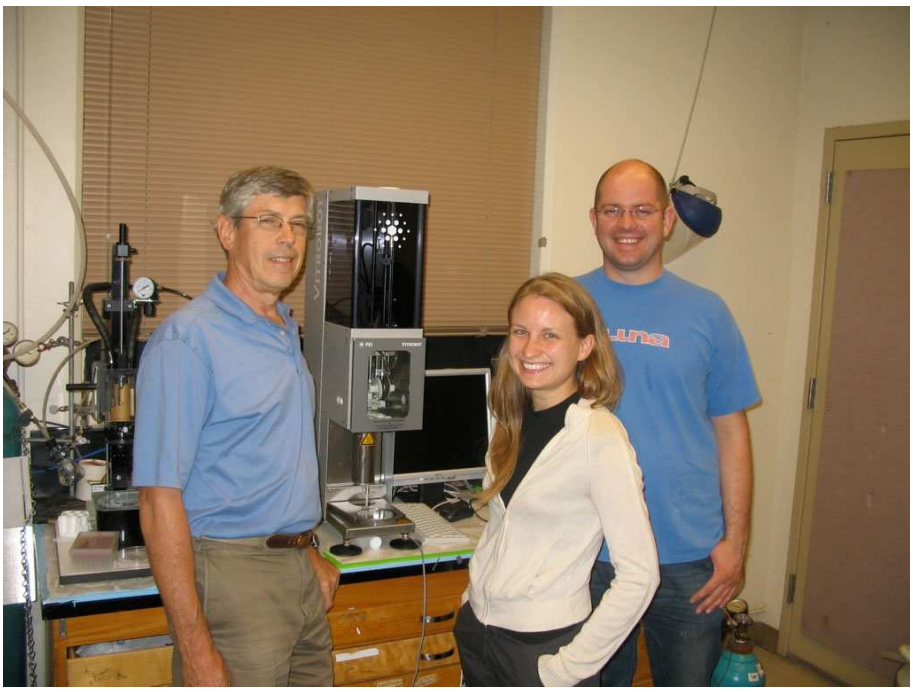

Figure 3.2: Pictures of the FEI Vitrobot with Ken Downing (left), Bjorg Larson (center), and Andrew Stewart (right).

Blotting offset	2 mm
Blotting time	3.5 s
Humidity	80%
Waiting time	120 s

Table 3.1: Vitrobot parameters and settings.

table, with solution facing up, for a couple of minutes to improve the chance for cells to stick on the formvar. Next, we mount the grid onto the tweezers of the Vitrobot. Table 3.1 lists the typical parameters and condition settings of the Vitrobot for our experiment. Although it is easy to determine the vitreous ice formation in EM, it is difficult to determine the quality of the ice layer in soft x-ray microscopy due to its large wavelength (2.4 nm for 520 eV x-rays). Through numerous trials with different conditions, this list gives to our knowledge the most suitable settings for yeast cells and spores. The Vitrobot will follow the settings once they are stored in the control system. First the robot lets the sample sit for a while (the waiting time); then it blots the sample at a certain offset position for some seconds (blotting time). A too-high offset will leave too much water on the grid and result in a too-thick ice layer, while too low an offset tends to lead to rips in the formvar coating. In our case, an offset of 2 mm with 3.5 s blotting creates a uniform ice layer of about 1 μm thick. After blotting, the grid is automatically plunged into liquid ethane for fast cooling, at which point the grid can be removed from liquid ethane. To avoid warming above the -135°C recrystallization temperature, the grid is then transferred through cold nitrogen gas to a liquid nitrogen storage dewar.

One thing that need to be mentioned here is that the yeast cells, especially the spores, tend to stick together. Since we have strict support constraint and a

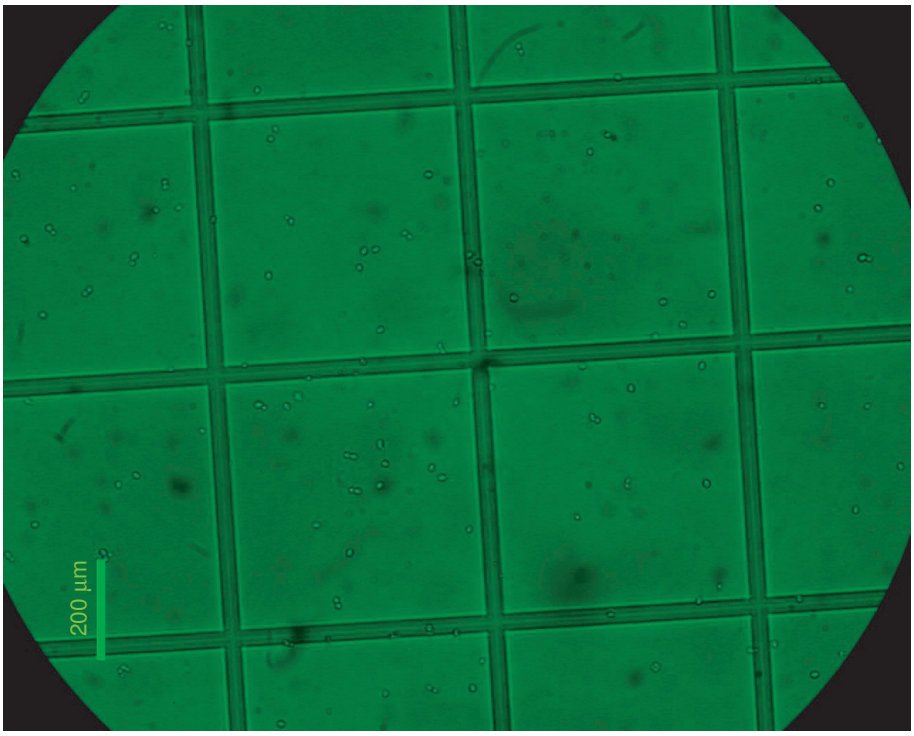

Figure 3.3: Visible light micrograph of a cellometer with yeast spores on it. An average of 15 cells per square indicate a good concentration for plunging.

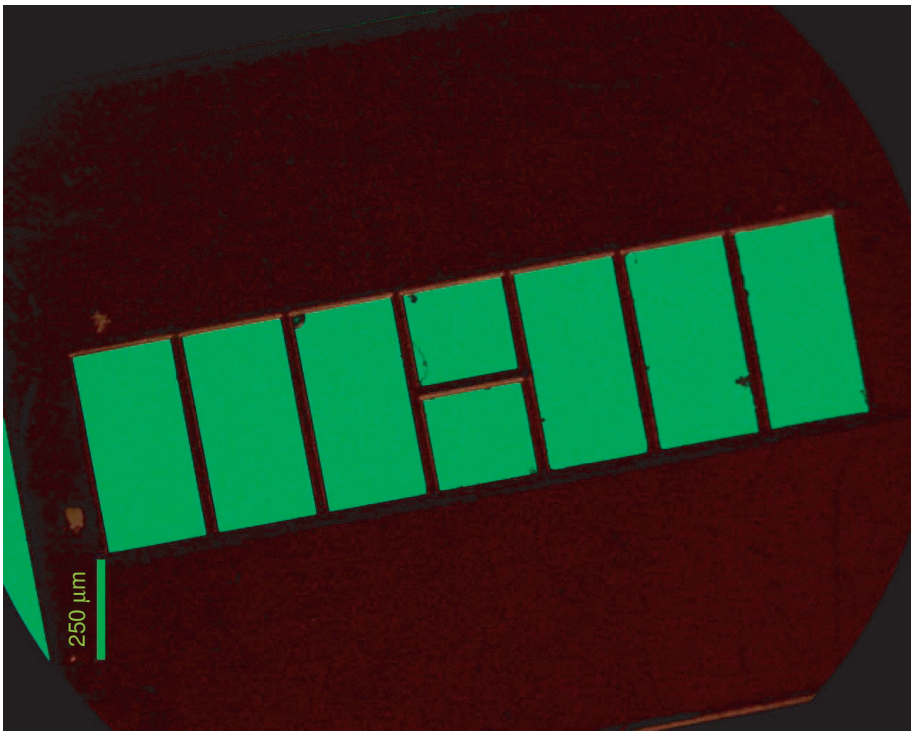

Figure 3.4: Visible light micrograph of a formvar coated copper grid with yeast cells on it. Cells are too small to be seen with this magnification.

preferable sample size imposed by the coherence of the beam (see discussions in Chapter Two), we hope to image single cells rather than a big clump. Once we tried to sonicate the cell solution right before plunging; however, this method appeared to be tricky. If the sonicating power is not high enough, the cells are not going to separate very well. But when the sonicating power is a little too high, the vibration can destroy the cell's inner organelles, and sometimes even the cell walls. Most recently, we have been shaking the solution with a vortex mixer before plunging. The problem is not completely solved, but at least a couple of good cells can be found on every successfully plunged grid.

There is no guarantee that this plunging method will produce vitreous ice layer though. It is possible for us to try high-pressure plunging at some point. High-pressure cooling was developed to vitrify millimeter-sized tissue samples, and more recently it has been developed for protein crystallography studies. In this approach, the sample is first pressurized to 100-200 mbar, after which point it can be frozen without crystalline ice formation; afterwards the pressure can be brought down to 1 atmosphere without a change in non-crystallinity [47]. High pressure cooling worked very well for crystallography. Fig. 3.5 shows the diffraction patterns of a crystal flash-cooled at ambient pressure and pressure-cooled at 130 MPa, respectively. There are no evident ice rings in the diffraction pattern of the pressure-cooled sample, while strong ice rings are present in the diffraction pattern of the sample cooled without high pressure, so that the Bragg peaks can hardly be seen there. It is not clear that our cells need to be plunged under high pressure since they are smaller than those protein crystals. But if we do encounter problems with vitreous ice production, it may be worthwhile to try this technique.

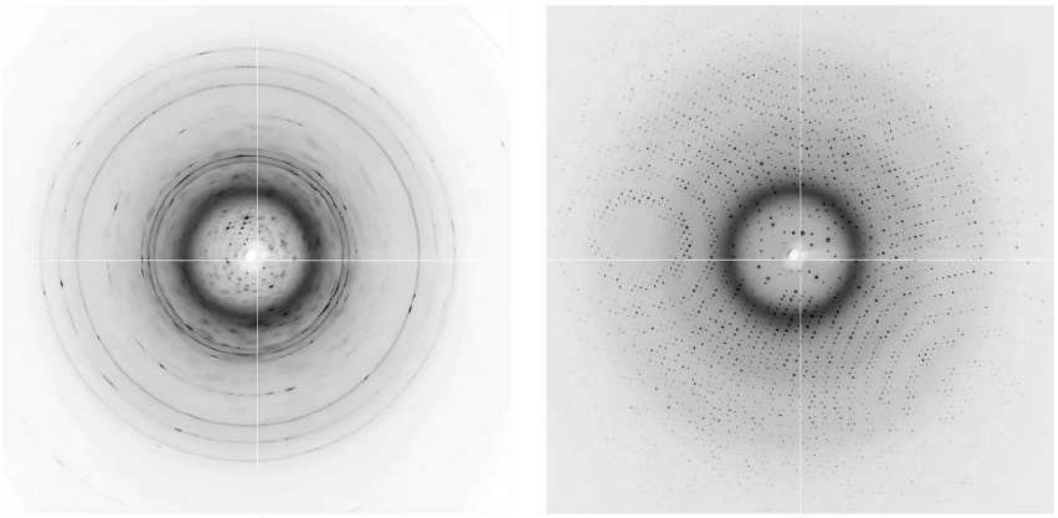

Figure 3.5: Left: x-ray diffraction pattern of a crystal flash-cooled at ambient pressure, where strong ice rings are seen. Right: x-ray diffraction pattern of the same crystal pressure-cooled at 130 MPa, with no visible ice rings [47].

3.3 Sample Transfer

One of the critical steps in having a good specimen in the beam is to quickly transfer the sample from the liquid nitrogen storage dewar to the vacuum chamber, since during this procedure, the specimen is inevitably exposed to the room temperature air, and the humidity in the air could easily settle down onto the grid and become ice crystals. To minimize the ice accumulation during sample transfer, we developed a few techniques/tricks in this procedure [48]. The sample is mounted onto a Gatan 630 cryo-holder (See Fig. 3.6) at the cryo-workstation. The whole process is done under liquid nitrogen and cold nitrogen gas environment. To avoid frosting from the tremendous amount of water molecules exhaled in our breath, we now wear a transparent plastic mask while working with the cryo-sample. Once the sample is mounted onto

the holder, it needs to be transferred to the vacuum chamber. This is the part in which some brief exposure to the room temperature air occurs. Although the grid is retracted into the slot on the tip of the holder so that it is shielded from the environment, ice accumulation can still happen. To minimize the chance for ice crystals to form during the transfer, we immerse the tip of the holder in a cup of liquid nitrogen. Before inserting the holder into the airlock of the vacuum chamber, we pump the airlock down, and then vent it with dry nitrogen gas.

Figure 3.6: A picture of the Gatan 630 Cryo-holder with a enlarged view of its tip with grid in.

3.4 Ice Formation in the Vacuum Chamber

In spite of our use of the procedures described above, as of the end of 2007 we had not yet obtained any promising reconstructions of frozen-hydrated cells. We may, however, find the explanation in one of our experiments in

November 2007. What we did then was to insert a dry empty formvar coated grid into the vacuum chamber, and cool it down with the liquid nitrogen. After the temperature of the grid stabilized at around $-160°$C, we took its diffraction pattern every minute. Surprisingly, after certain time of waiting, a doughnut-shaped ring clearly appeared in the pattern. We repeated the experiment several times and found that the formation of this ring is independent of the grid condition, which eliminates the possibility that the formation of the "doughnut" is due to formvar degradation in the beam. Moreover, the time for this ring to form is highly dependent on the vacuum pressure in the chamber. One of the experiments was done at a base pressure of about 3×10^{-6} Torr; Fig. 3.7 shows the diffraction pattern of the grid before cooling and one hour after cooled to $-160°$C. Another experiment done at about 1×10^{-7} Torr shows that the "doughnut" formed at a much slower rate. On the left of Fig. 3.8 we show the diffraction pattern of the room temperature grid, and on the right is the diffraction pattern of the grid kept at $-160°$C for one hour. While the formation rate of the "doughnuts" was very different, their extent and shape in Fourier space are essentially identical. We have reasons to believe that the "doughnut" is due to the scattering from either the ice crystals formed in the chamber, or a "wavy" surface of an amorphous ice layer. Since the grid is the coolest point in the chamber, water vapor molecules have a good chance to stick onto it when they hit it. Ice crystals could form when more water molecules are stuck on the grid. Since it takes more than one hour to collect the data (especially when going to 3D imaging the data collection time could be well over several hours), this scattering from ice formed during data collection could prevent us from reconstructing diffraction patterns using a finite

support constraint, since the "empty" ice area outside the cell might not be so optically empty to the x-ray beam.

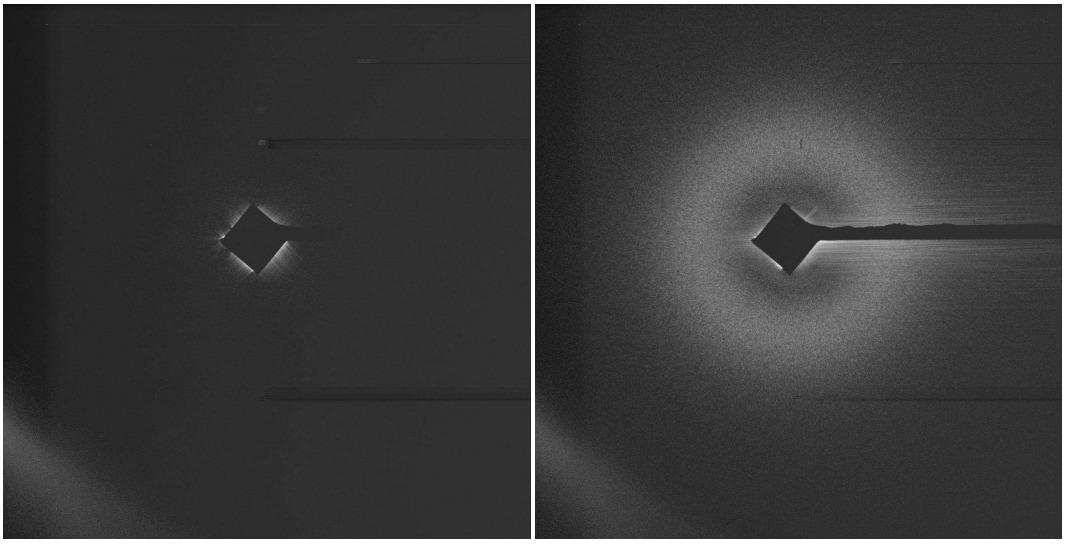

Figure 3.7: Diffraction patterns of empty formvar coated grid before cooling down (left) and one hour after being kept at $-160°$C (right). These diffraction patterns extend out to a maximum spatial frequency of 35.8 inverse microns at the center of the right edge. Chamber pressure was about 3×10^{-6} Torr.

From the radius of the ring, one can calculate the corresponding size of the scattering objects in the real space. From the November 14th's data, shown in Fig. 3.7, we have the inner radius of the doughnut to be $r_0 = 2.96$ mm, and the outer radius to be $r_1 = 7.44$ mm. The corresponding spatial frequencies can be obtained as

$$f_0 = \frac{r_0}{\lambda z} = 7.98\ \mu\text{m}^{-1} \tag{3.1}$$

$$f_1 = \frac{r_1}{\lambda z} = 12.29\ \mu\text{m}^{-1}\,, \tag{3.2}$$

where $\lambda = 2.38$ nm is the wavelength for 520 eV, and $z = 15.56$ cm is the

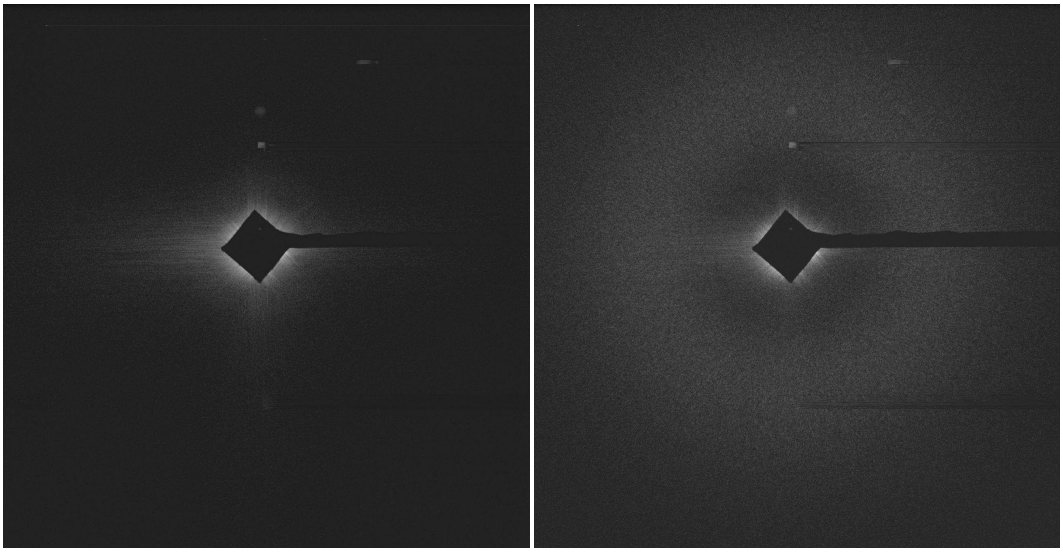

Figure 3.8: Diffraction patterns of empty formvar coated grid before cooling down (left) and one hour after being kept at $-160°$C (right). Chamber pressure was about 1×10^{-7} Torr.

distance from sample to CCD. Therefore, the corresponding scattering length in real space is between 50 to 100 nm.

We have made several attempts to understand the structure of the ice crystals, although no conclusive explanation has yet been arrived at. Our first idea was that it is reasonable to assume that the ice non-uniformities have a Gaussian shape. We did a simulation, in which a number of little Gaussian ice bumps were placed randomly on a grid. However, its diffraction pattern shows a Gaussian type distribution too. In fact, theoretically we can also prove that the Fourier transform of many randomly located Gaussian functions with different amplitudes and widths is another Gaussian. The amplitude and width of this new Gaussian can be calculated accordingly. Next, we thought the donut shape could be described by two Gaussian functions, with one of

them having negative magnitude. However, it seems to be unnatural to have an "inverted Gaussian" in the structure. Finally, we simulated circular ice bumps or ice bumps with other shapes, but the diffraction patterns always show a sharp edged ring, instead of a donut shape.

The next question would be how can we avoid or at least minimize the ice accumulation in data collection. Several different generations of anti-contamination device (ACD) have been developed in our group. The first version, called the "cold finger," was just a large piece of copper plate mounted in the chamber, several centimeters away from the sample. It does significantly improve the chamber pressure (about one order of magnitude lower after cooling the cold finger); however, it does little in protecting the sample from being hit by the residual gas molecules. In addition, there are several other versions developed later on to help protecting the specimen, which basically introduce a small copper plate right in front of the sample with a hole in the center to let the beam pass. It is in general a difficult task to mount and align such a device given the small operation space in the chamber. After cooling, the material is contracted and stiff, and it is not easy to align them at room temperature while predicting its exact position after cooling. But significantly less ice accumulation was detected once the ACD is in position.

An even better ACD would be a closed copper box, with two holes in the beam path. This configuration has been adopted in some groups [49]. With a "cryo box" that when inserted completely shields the specimen with apertures 0.5 and 0.8 mm in diameter above and below the specimen holder, respectively, they achieved a contamination rate of 1.3 $\mathring{A}$/h on vitreous ice, which is very encouraging for imaging of cryo-samples.

Chapter 4

Centering the Diffraction Data

X-ray diffraction microscopy offers a way to image a single object in 3D. However, one of the major challenges when processing the data is to accurately determine the zero spatial frequency position. In this chapter, simulations of reconstructing shifted data show that if the center of a 2D diffraction pattern is shifted by more than 3 pixels from its true center, the positivity constraint to the phase, which otherwise might be applied to improve the convergence of the reconstruction algorithm, can not be imposed. Moreover, the phase unwrapping problem may appear during the reconstruction. These issues undermine the quality of the reconstruction of 2D data sets. Furthermore, differing shifts in each 2D diffraction pattern will lead to inconsistences when assembled into a 3D Fourier "cube" of data, making the 3D reconstruction very difficult. We developed a three-step method to precisely align the diffraction data. The first step is to use the power spectra of segments of a diffraction pattern to pre-align the data. By comparing the slopes of these power spectra, the shift of the alignment can be reduced to a couple of pixels. The second step is to

align the data with its autocorrelation. After the pre-alignment, the phase of the autocorrelation should not be wrapped. By comparing the real part and the imaginary part of the autocorrelation, we could then further align the data to one pixel precision. The third step is to align the data with an attempted reconstruction. The exact zero spatial frequency position can then be found by examining the linear ramp present in the reconstructed phase, when there is no phase wrapping involved.

4.1 The basic theories

In most X-ray diffraction microscopy experiments, a beam stop is used to block the incidence of the direct beam to protect the detector. Due to the projection of the beam stop, at the center of the diffraction pattern there are a certain amount of missing pixels. In our experiment this missing center is normally bigger than 200 pixels. The data array has a dimension of 1340×1300 pixels and the beam size is about 20 pixels in diameter. During data assembly, the estimated position of the center of the diffraction pattern can be several pixels away from the real center. In simulations we have found that with 2D data sets, in most cases if the shift is more than 3 pixels in either the x or the y direction, we can not impose the positivity constraint to the phase in reconstruction. This may lead to a slower convergence of the algorithm. However more seriously, the phase part will be wrapped. The array used in the simulations is 512×512 pixels. As the shift becomes 3 pixels or more, the phase of the reconstruction will exceed 2π. In fact with a shift of 8 pixels in the simulation, we see that the retrieved phase goes to 6π. In reality the array size

is bigger, which may result in the wrapping occurring even at smaller shifts. It is difficult to unwrap the phase when wrapping occurs in a large portion of the reconstructed phase. When going to 3D X-ray diffraction microscopy, this shift in each 2D data set will make it impossible to properly assemble the 3D data cube, which in turn will render the reconstruction of a 3D object very difficult. So here we develop a way to find the exact zero frequency position in 2D data sets.

4.1.1 The Power Spectrum Method

If we look at the angular segments of a perfectly centered diffraction pattern, as shown in Fig. 4.1, the power spectral densities of both left and right segments on a log-log scale should be straight lines with identical slopes. When it is not perfectly centered, the power spectrum of the left segment will have a different slope from the one of the right segment. The same from the top segment relative to the bottom segment. In Fig. 4.1, in the left half diffraction pattern, we take $+150^\circ$ to $+210^\circ$ into account; and in the right half diffraction pattern, we consider -30° to $+30^\circ$. By examining the slopes of the power spectra of the left, right, top and bottom segments of the diffraction pattern we will be able to tell how to re-center the data. The method can reduce the misalignment of the zero frequency position to a couple of pixels, in which case an autocorrelation or a reconstruction without heavily wrapped phase is possible.

How big should this angular segment be? When we went from 60° range as shown in Fig. 4.1, to a 180° range (*i.e.*, a half plane), the calculated center

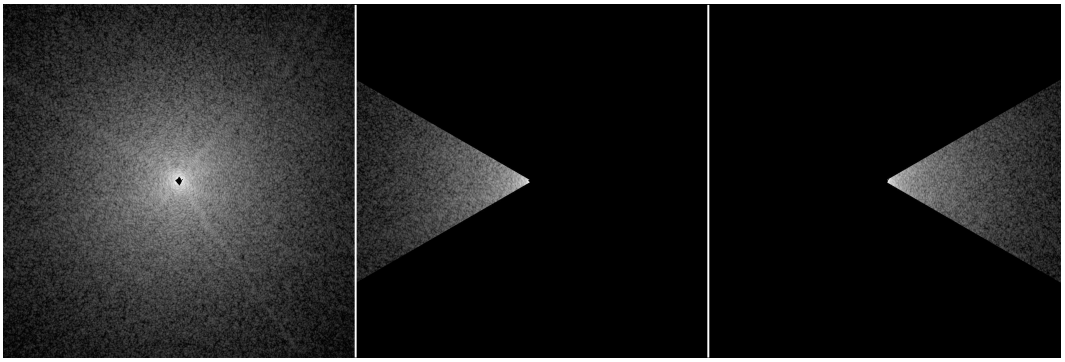

Figure 4.1: (a)Full diffraction pattern of a freeze-dried yeast cell, data collected and assembled by Shapiro [20]; (b)+150° to +210° angular segment of the pattern; (c)−30° to +30° angular segment of the pattern.

position changed by only two pixels. If we take account the shift in both x and y directions, using a 90° angular segment will give us more sensible results. In the rest of this chapter, we are going to stick with the analysis of 90° angular segments. This means taking −45° to +45° data for calculating the left power spectrum; +135° to +225° for the right one; +45° to +135° for the top one; and −45° to −135° for the bottom one.

4.1.2 The Autocorrelation Method

After being pre-aligned with the power spectrum method, the data center can still be a couple of pixels away from its zero spatial frequency position. We can then use the autocorrelation method to re-align the data.

The autocorrelation of an arbitrary function $f(\vec{x})$ is defined as following:

$$R(\vec{x}) = \int d\,\vec{x}'\; f(\vec{x} + \vec{x}')f^{\star}(\vec{x}') \tag{4.1}$$

In diffraction imaging, the autocorrelation of the exit wave $f(\vec{x})$ is just the inverse Fourier transform of the diffraction pattern intensity $|F(\vec{k})|^2$:

$$\begin{aligned}
\mathcal{F}^{-1}(|F(\vec{k})|^2) &= \int e^{2\pi i \vec{k}\cdot\vec{x}} d\ \vec{k} \int f(\vec{x'}) e^{-2\pi i \vec{k}\cdot\vec{x'}} d\ \vec{x'} \int f^{\star}(\vec{x''}) e^{2\pi i \vec{k}\cdot\vec{x''}} d\ \vec{x''} \\
&= \int d\ \vec{x'} \int d\ \vec{x''}\ f(\vec{x'}) f^{\star}(\vec{x''}) \delta(\vec{x} - \vec{x'} + \vec{x''}) \\
&= \int d\ \vec{x'}\ f(\vec{x} + \vec{x'}) f^{\star}(\vec{x'}) \qquad (4.2) \\
&= R(\vec{x})\,.
\end{aligned}$$

When the diffraction intensity is perfectly central symmetric, its autocorrelation is real. We can denote the diffraction pattern as $f(r)$, which is real at any r. Now, we are going to show that its inverse Fourier transform is also real.

$$\mathcal{F}^{-1}(f(r)) = \int_0^{\infty} f(r) r dr \int_0^{2\pi} d\phi\ e^{ir(k_1 \cos\phi + k_2 \sin\phi)} \qquad (4.3)$$

The possible imaginary part comes from the integral on ϕ. We apply a Taylor expansion to the exponential part, and rewrite the integral on ϕ as

$$\sum_{n=0}^{\infty} \int_0^{2\pi} d\phi \frac{(ir)^n}{n!} (k_1 \cos\phi + k_2 \sin\phi)^n \qquad (4.4)$$

When n is even, the terms in Eq. 4.4 is automatically real. Next we are going to consider the case when n is odd. Applying a polynomial expansion to Eq. 4.4,

we have the odd terms of

$$\begin{aligned}
&\frac{(\imath r)^n}{n!}\int_0^{2\pi} d\phi\Big(\frac{k_1-\imath k_2}{2}e^{\imath\phi}+\frac{k_1+\imath k_2}{2}e^{-\imath\phi}\Big)^n \qquad (4.5)\\
&\quad=\frac{(\imath r)^n}{n!}\sum_{m=0}^{n}\Big(\frac{k_1-\imath k_2}{2}\Big)^m\Big(\frac{k_1+\imath k_2}{2}\Big)^{n-m}\binom{n}{m}\int_0^{2\pi} d\phi\; e^{\imath m\phi}e^{-\imath(n-m)\phi}\\
&\quad=\frac{(\imath r)^n}{n!}\sum_{m=0}^{n}\Big(\frac{k_1-\imath k_2}{2}\Big)^m\Big(\frac{k_1+\imath k_2}{2}\Big)^{n-m}\binom{n}{m}\int_0^{2\pi} d\phi\; e^{-\imath(n-2m)\phi}\\
&\quad=\frac{(\imath r)^n}{n!}\sum_{m=0}^{n}\Big(\frac{k_1-\imath k_2}{2}\Big)^m\Big(\frac{k_1+\imath k_2}{2}\Big)^{n-m}\binom{n}{m}\;2\pi\;\delta_{n,2m}\,,
\end{aligned}$$

where $\binom{n}{m}=\frac{n!}{(n-m)!m!}$. Obviously, when n is odd, the delta function is zero, so all the terms with odd n's are zero. Therefore, the autocorrelation of a perfectly centrally symmetric intensity pattern is pure real.

With this result, we can try to center the data by minimizing the imaginary part in the autocorrelation. This is easiest to do when the phase is not wrapped around 2π. So it is feasible when the shift in the data is relatively small, say one or two pixels. That is why the first step, using the power spectrum to pre-align the pattern, is of importance.

4.1.3 The Reconstruction Method

The autocorrelation method is capable of aligning the data with one pixel precision. However, even half pixel misalignment could make the 3D assembly rather difficult. How can we correct this? From the shift theorem of Fourier

transforms we know that a linear shift in real space will result in a phase shift in reciprocal space. In 1D, this is to say

$$\mathcal{F}\{g(x-a)\} = e^{-\imath ka} G(k)\,, \tag{4.6}$$

where

$$\mathcal{F}\{g(x)\} = G(k)\,. \tag{4.7}$$

Similarly, if a shift is introduced into the reciprocal space, a linear phase ramp would be expected in the real space. In our case which is in 2D, this can be written as

$$\mathcal{F}^{-1}\{G(k_x-a, k_y-b)\} = e^{\imath(ax+by)}\, g(x,y). \tag{4.8}$$

This linear phase shift $ax + by$ is dominant compared to the phase change caused by the specimen. In our experiment the specimen is a biological cell. We shall be able to do a linear plane fit on the reconstructed phase and find a and b, once a reasonable reconstruction is obtained. Fig. 4.2 is the horizontal scan line crossing the middle of a retrieved phase from the data in Fig. 4.1 shifted by 1 pixel in both x and y directions. The linear phase ramp is evident compared to the small features inside the biological specimen.

This method can determine the zero frequency position exactly. However, when the shift is large (say more then 3 pixels in either the x or the y direction), the phase ramp will be big enough to drive the phase of the object over 2π. Then we will have to unwrap the phase before being able to apply the phase ramp approach. Since the unwrapping is not always easy when dealing with real data sets, it is necessary to use the power spectrum density method and

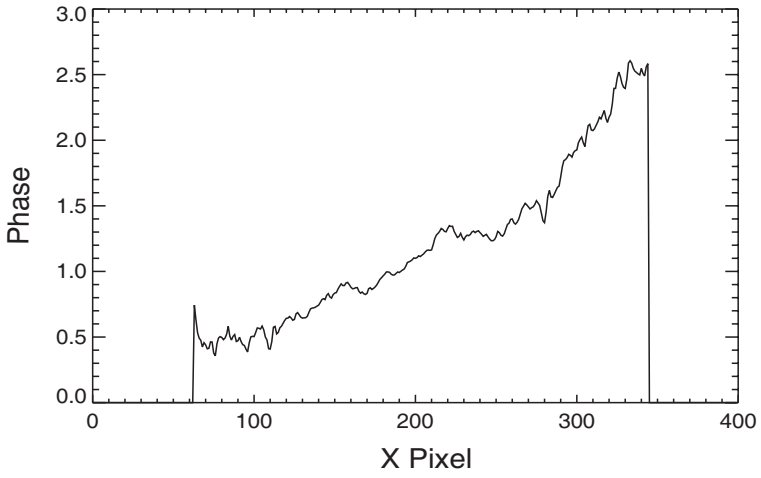

Figure 4.2: The horizontal scan line crossing the middle of the retrieved phase from the diffraction data of a freeze-dried yeast cell (data collected and assembled by D. Shapiro) shifted by 1 pixels in both x and y.

the autocorrelation method to pre-align the diffraction pattern to avoid serious phase wrapping problem.

In the rest of the chapter, we are going to discuss these three steps in detail with both simulated data and real data sets.

4.2 Power Spectrum Method

We divide the diffraction pattern into top half, bottom half, left half and right half and take angular segments of 90° into account. If the zero frequency position is determined correctly, we expect that the slopes of the power spectra of the top and bottom data are equal, and the slopes of the power spectra of the left and right data are equal too.

First, we will try to apply this method to the simulated cell in Chapter Two. Again, it is a cell-like protein object in an ice cube. The dimension of

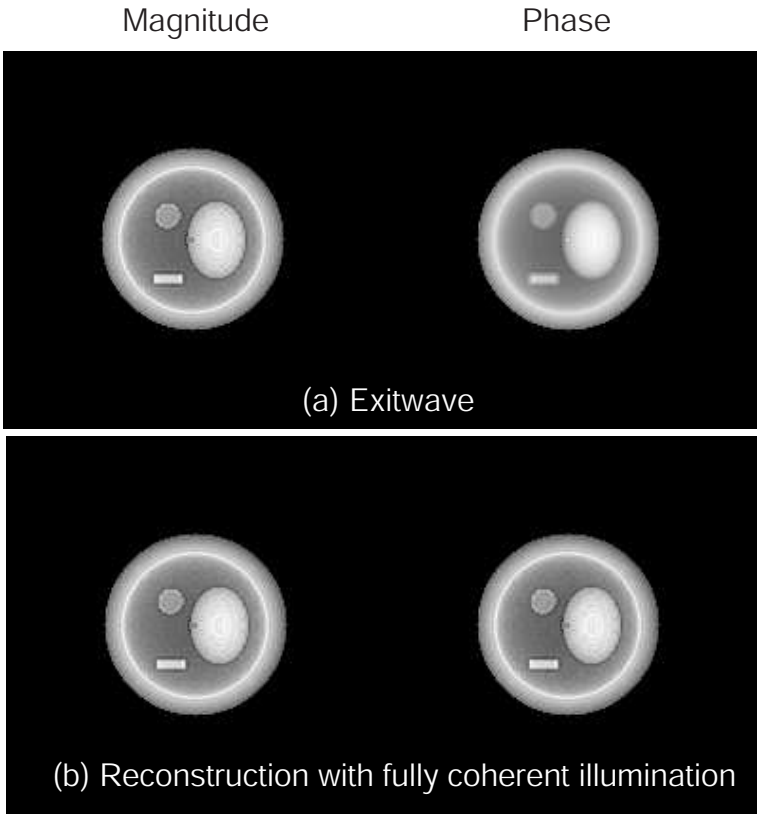

Figure 4.3: (a) Exit wave of the fake cell consisting of lipid membrane, soluble protein and protein bulks inside the cell; (b) the reconstruction of its not shifted diffraction pattern obtained by using difference map method.

the cube is $512 \times 512 \times 512$ pixels, the diameter of the fake cell is 100 pixels, and the voxel size is $(2\ \text{nm})^3$. The membrane of the cell is made by lipid. The cell is filled with soluble protein and has one ellipsoid protein bulk and two protein cylinders inside. Suppose the x-ray beam illuminates along the z axis. The center of the cell was located on the exit plane of the ice cube along the z axis, which is set to be the focal plane, and the protein structures were cut off by this focal plane. Thus, only half of the cell remains in the cube.

To simulate the exit wave on the focal plane, the ice cube is cut into a

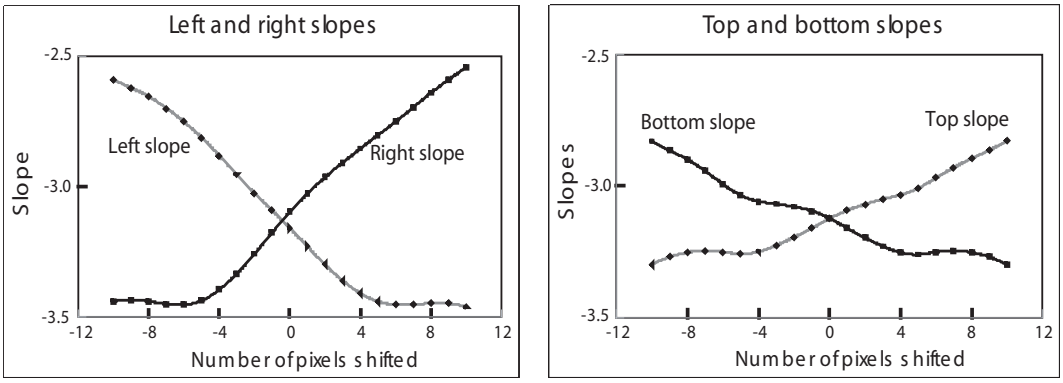

Figure 4.4: Slope curves of the power spectra of the fake cell. The left and right slopes cross at about -0.2 pixels, which indicates the real center is 0.2 pixels to the left; and the top and bottom slopes cross at almost right at 0 pixels, which indicates the real center is right there in vertical.

series of thin slices perpendicular to z axis. The diffraction pattern after each slice is propagated to the one behind it. In the simulations, the exit wave is generated with 10000 incident photons per pixel, and the CCD dark current and photon noise are added to obtain the final diffraction pattern.

Fig. 4.3 shows both the magnitude and phase of the exit wave and the reconstruction of the perfectly centered diffraction pattern. The reconstruction has been done by using the difference map method [24].

By plotting the slopes of the power spectra of every segment (the left, right, top and bottom data) while shifting the diffraction pattern by 10 pixels in each direction horizontally with step size equals to one, we find that both curves (left and right curve, top and bottom curve) cross right at the zeroth pixel position, as shown in Fig. 4.4. This is a good confirmation that the data is well centered.

Next, let's look back at the real data set shown in Fig. 4.1 which is collected

and assembled as a 1200 × 1200 array by D. Shapiro [20]. It is a diffraction pattern of a freeze-dried yeast cell. This data set has been successfully reconstructed [20][50]. Now we try to use the power spectral density method to examine the zero frequency position of this data. Fig. 4.5 shows the top and bottom power spectra of the original data and of the data shifted by 10 pixels in the +y direction. The two power spectra of the original data have a very similar behavior, while the ones of the data shifted 10 pixels to the top differ from each other. Since the data was shifted to the top, the top and bottom power spectra show a difference in slopes. The shaded areas are used for linear fits to obtain the slopes. To illustrate this further, we plot the percentage difference from the average of top and bottom power spectra in Fig. 4.6. Again after shifting, the difference in the power spectra is evident.

We tried to shift the data in +x, -x, +y and -y directions by 10 pixels, respectively. (Plus sign is shifted to the right/top.) The slopes of each shifted data have been recorded. The results are shown in Fig. 4.7. The left and right slope curves cross at about -0.8 pixels, and the top and bottom slope curves cross almost right at the zeroth pixel. This shows that the data was very well aligned. We are confident that the center of the diffraction pattern is not more than one pixel shifted in either direction.

In general, by looking at the power spectrum density of the diffraction pattern, we could reduce the shift in the data to less than a couple of pixels.

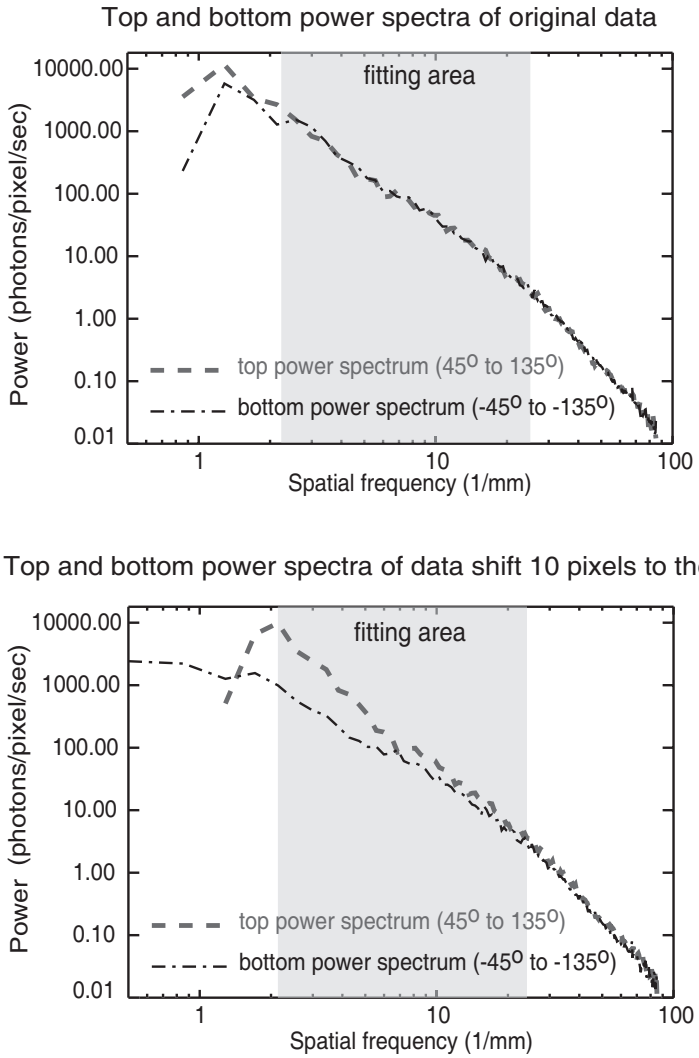

Figure 4.5: Power spectral densities of the original diffraction data from a freeze-dried yeast cell (data collected and assembled by D. Shapiro), and the data shifted by 10 pixels in the +y direction.

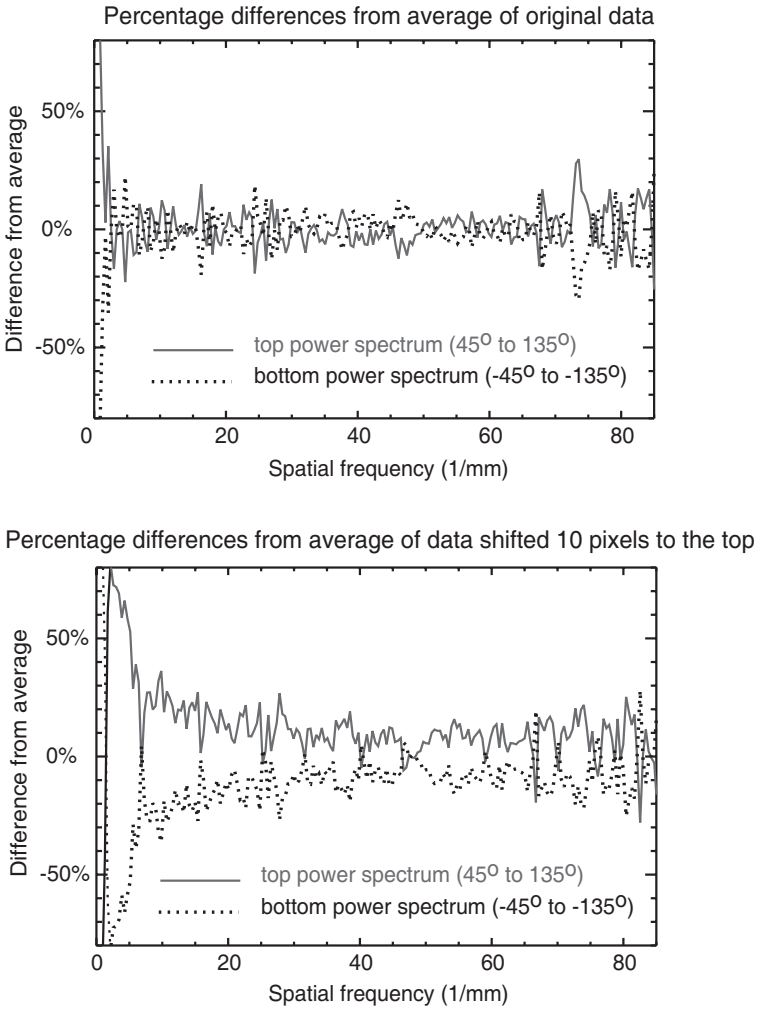

Figure 4.6: Percentage differences from average of the power spectral densities of the original diffraction data from a freeze-dried yeast cell (collected and assembled by D. Shapiro) and the data shifted by 10 pixels to the top.

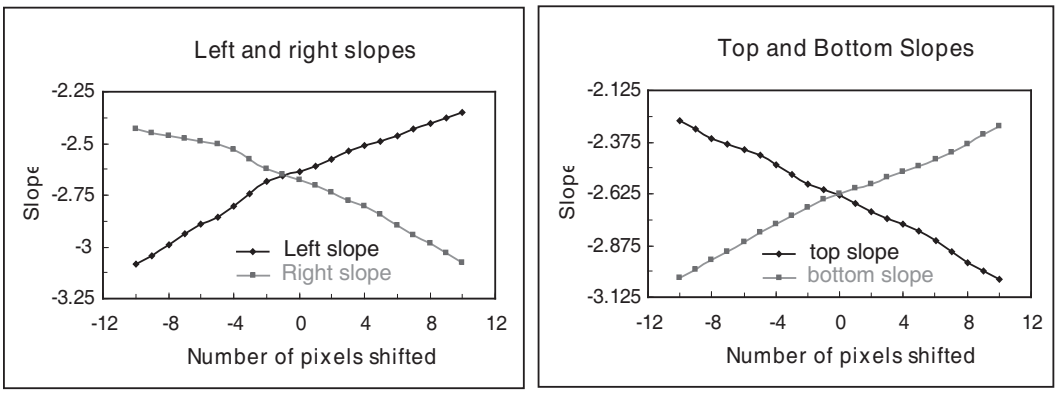

Figure 4.7: Slope curves of the power spectra of a freeze-dried yeast cell (collected and assembled by D. Shapiro). The left and right slopes cross at about -0.8 pixels, which indicates the real center is 0.8 pixels to the left; and the top and bottom slopes cross at about -0.1 pixels, which indicates the real center is 0.1 pixels to the bottom. Since the shifts in both x and y directions are less than one pixel, so that we think this data is very well centered.

4.3 Autocorrelation Method

Now, we are going to apply the autocorrelation method to check the zero spatial frequency position in both the simulated data and the real data discussed in the last section. We shift the data by one or two pixels in each direction horizontally, and record the ratio of the total imaginary part over the total real part. Fig. 4.8 shows the plots of the ratios versus the shifted pixel numbers with simulated data and real data set. As expected, when it's well-aligned, the autocorrelation of the simulated data is almost pure real. As the shift gets bigger, the degree of complexity increases significantly. The autocorrelation of the well-aligned real data also appears at the local minimum of the curve; however, it still shows some degree of complexity. The plot suggests that the true zero spatial frequency position of the real data is about 0.4

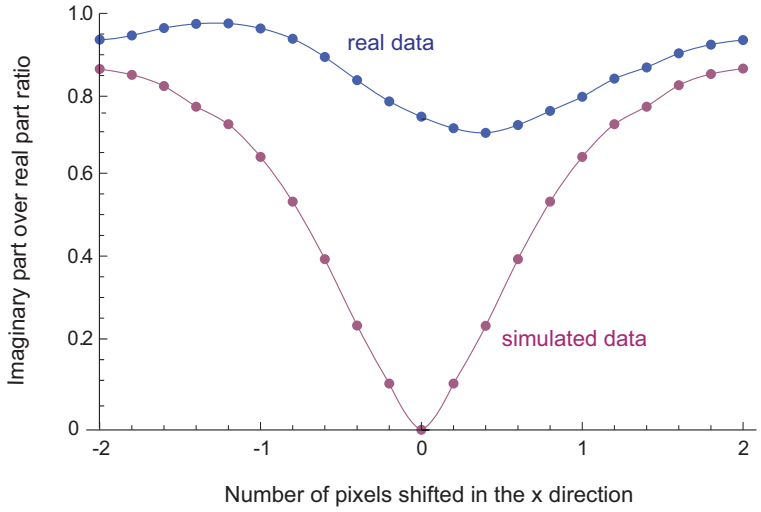

Figure 4.8: Plot of the imaginary to real part ratios versus shifted pixel number in the x directory (shift step size = 0.2 pixels). In the plots of both simulated data and real diffraction data from a freeze-dried yeast cell (collected and assembled by D. Shapiro), a local minimum appears at the center position, although the autocorrelation of the well-aligned simulated data is of a much less degree of complexity when compared to the well-aligned real data. The plot suggests that the real data has a center about 0.4 pixels to the left of the true zero spatial frequency position, and the simulated data is well-centered.

pixels right to the center of the assembled data, while the simulated data has a center right at its zero spatial frequency position.

Since a high-pass filter has to be applied to render the hard edge of the beam stop projection to generate an autocorrelation, which may influence the analysis, the accuracy of the estimated center of the data is around 0.2 pixels.

4.4 Reconstruction Method

After the pre-alignment with the power spectral density method and the autocorrelation method, we can then re-center the data precisely by fitting

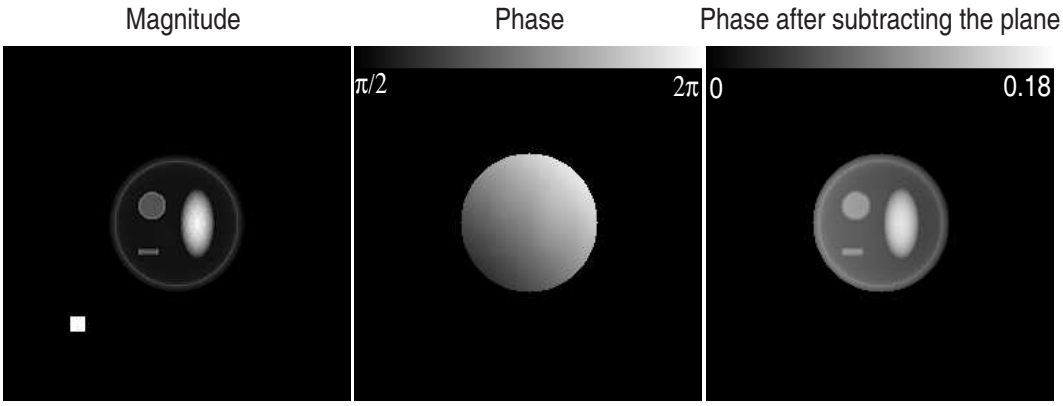

Figure 4.9: Reconstructions of the diffraction pattern of a simulated cell-like object shifted by 1 pixel in both the x and the y directions. The left image shows the reconstructed magnitude; middle one is the retrieved phase in which a linear phase ramp is evident; the right one is the phase after subtracting the fitted phase ramp plane in which detailed features of the "cell" appear again.

the linear phase ramp in the reconstruction. Below, we will discuss the phase ramp method further with some simulations and also with real data.

4.4.1 Simulations

Simulations have been done with up to 10 pixels shifted in the x or the y directions in the diffraction pattern without missing pixels at the center.

In Fig. 4.3 we see both the magnitude and phase of the exit wave and the reconstruction of the perfectly centered diffraction pattern. Fig. 4.9 shows a sample reconstruction of a shifted diffraction pattern. This pattern has been shifted by 1 pixel in both the x and the y directions. If we do a plane fit of the phase ramps, the resulting slopes suggest that the shift in the x direction is 1.013 pixels, and the shift in the y direction is 1.002 pixels.

To explore the method systematically, we shift the diffraction pattern from

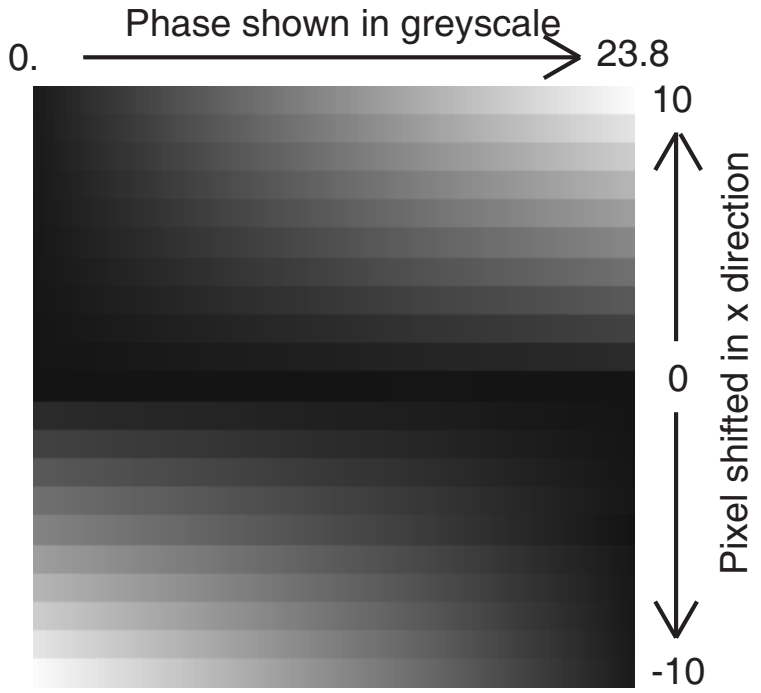

Figure 4.10: Horizontal scan lines across the middle of retrieved phases of the diffraction pattern of a simulated cell-like object, shifted from -10 to +10 pixels in the x direction.

1 pixel to 10 pixels in both + and - x directions with a step size of 1 pixel. Fig. 4.10 shows the scan lines across the middle of the retrieved phases of these shifted diffraction patterns. It illustrates the change of the phase ramp corresponding to different shifts. A plane fit on these reconstructed phases finds back exactly the direction and the number of pixels shifted.

However, when the shift is more than 3 pixels, we do encounter the phase unwrapping problem. It is relatively easy to unwrap the phase in this simulation. But it is not so straightforward when dealing with real data. That makes the pre-alignment with power spectral density and autocorrelation very important.

4.4.2 Real Data

In section 4.2 we have checked the centering of the diffraction pattern of a freeze-dried yeast cell with the power spectral density method. In this section we are going to analyze the same data with the phase ramp method.

With a least square plane fit on the retrieved phases, we find the slopes in both the x and the y directions to be less than one pixel. The relative shifts are 0.47 pixels to the right, and 0.43 pixels to the bottom. The shift in the x direction agree with the results from the autocorrelation method. The reconstruction is shown in Fig. 4.11, (a). If we shift the data by 2 pixels to the right and 1 pixel to the top, we find the reconstruction algorithm converges much slower. The retrieved phase shows a clear ramp. Fig. 4.11, (b) is the reconstructed magnitude and phase of the shifted data. A plane fit on the phase shows that the shifts are 2.17 pixels to the right and 0.51 pixels to the top. Therefore, the results of the fit agree with our expectation very well.

Again, to illustrate the method further, we shift the data manually from -3 to +3 pixels in the x direction, with a stepsize of 1 pixel. Fig. 4.12 shows the horizonal scan lines across the middle of the retrieved phases of these shifted data.

The linear phase ramps here are not as smooth as the ones with simulated data. But they are good enough to get reasonable plane fits to indicate the position of the zero spatial frequency position.

Minor phase wrapping occurred when the shift reached 3 pixels. This did not affect the plane fit. Since a large portion of the phase array was not wrapped, we could just do a fit in that part of the array, excluding the edges

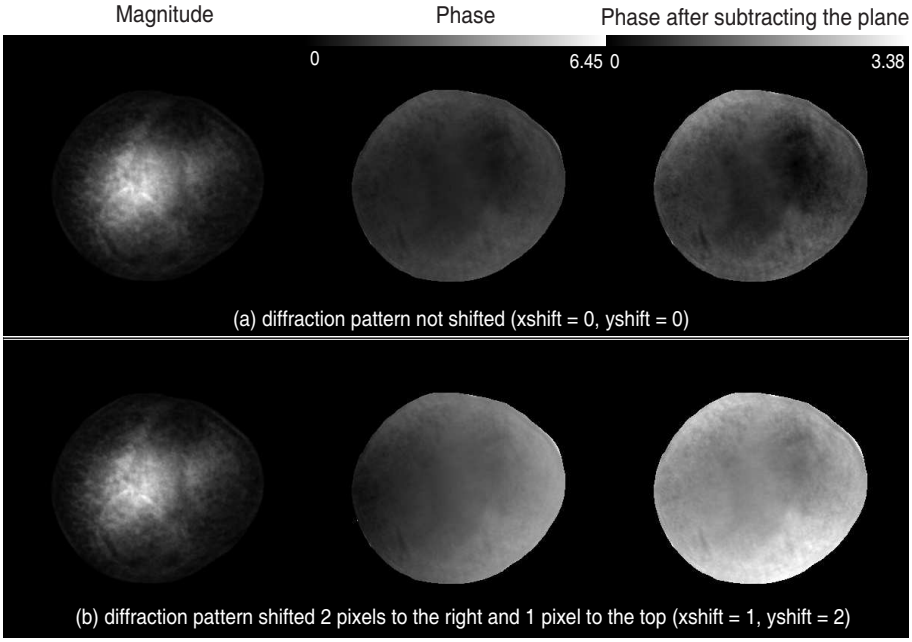

Figure 4.11: (a) the reconstructed magnitude and phase from the original data of a freeze-dried yeast cell (data collected and assembled by D. Shapiro); (b) the reconstructed magnitude and phase from data shifted by 2 pixels to the right and 1 pixel to the top.

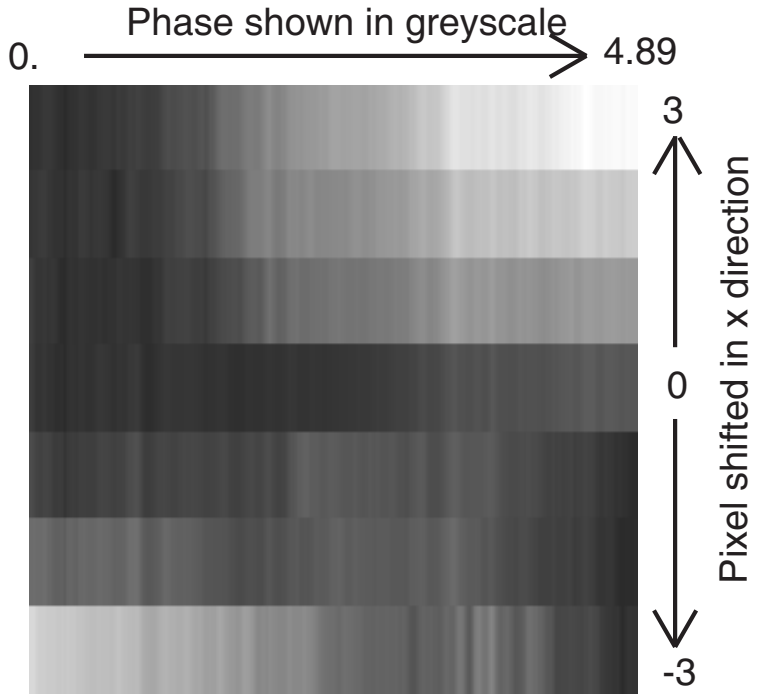

Figure 4.12: Horizontal scan lines across the middle of retrieved phases of the diffraction pattern of a freeze-dried yeast cell (collected and assembled by D. Shapiro) shifted from -3 to +3 pixels in the x direction.

in which phase wrapping occurs. The results of the fit look sensible.

4.5 Conclusion

Misalignment of the zero spatial frequency position in x-ray diffraction microscopy often causes difficulty in reconstruction. Here we presented a three-step procedure to correct the misalignment in data. By using the power spectral density method, we could reduce the misalignment to a couple of pixels. A reasonable autocorrelation without wrapped phase can be obtained after the pre-alignment. By minimizing the ratio of the imaginary part and the real part of the autocorrelation, we could further reduce the misalignment to within one pixel. Then to precisely align the data, we examine the linear phase ramp in the retrieved phases of the reconstruction. All the methods have been tested by both simulation and using real data sets.

In a 1200×1200 array, a 3 pixel shift may introduce wrapped phase in minor area. A linear plane fit on the unwrapped area of phase is still effective to find the zero spatial frequency position. However, when the shift is larger than 3 pixels, the wrapping may be severe, and it may be difficult to unwrap the phase with real data. Therefore, applying the power spectral density method to pre-align the data is necessary at the first stage of the assembly.

The second step is to check the complexity of the autocorrelation. Since a reconstruction is not always straight-forward, this method offers a possibility to align the data before a successful attempt of reconstruction is made.

The third step is to examine the linear phase ramp in the reconstruction. A reconstruction may not be easy to obtain, however, once we have it, this

method allow us to find the zero spatial frequency position exactly. This is of great use in 3D diffraction imaging.

The combination of the three methods completes the centering procedure in data assembly.

Chapter 5

Discussion and Outlook

In 2005, our group successfully reconstructed a freeze-dried yeast cell from its diffraction intensity collected at beamline 9.0.1 at the ALS in LBNL [20]. This proved that using a x-ray diffraction microscope to image biological samples is possible. However, given the tremendous merits of imaging wet cells, our efforts have moved towards imaging frozen-hydrated cells since then. So far no promising reconstruction has been obtained, but from all these experiences we have better understood the possible problems that one has to face when trying to image frozen-hydrated specimens, and this has led us to propose and study in detail possible resolutions to those problems.

First of all, given the coherence width at the sample, the specimen size often times is too big to be reconstructed. At early trials, our single yeast cells were between 5 to 7 μm. As we have seen in Chapter Two, without the de-convolution technique, the maximum size we can image is about 3 μm. Later on, we mostly used cells with size between 1 to 3 μm. However, it was difficult to get a single cell with clean background. Some of the good-

looking data, after several attempts, showed a bunch of cells sticking together, in which case a high resolution reconstruction showing the inner organelles becomes impossible. In the future, one of our foci should be how to produce single-cell samples so that the size of the specimen being imaged will stay within the coherence limit. Another possible way to deal with the problem is exploiting the de-convolution method as described in Chapter Two. This involves a detailed and accurate measure of the complex degree of coherence profile, which could be challenging itself. When de-convolving it from the data, special care needs to be taken at the low intensity pixels.

Secondly, we noticed that the ice contamination presents a big obstacle in our progress. Ice crystals may form during sample preparation, sample transfer, and even after the sample is in the vacuum chamber during the data collection process. As discussed in Chapter Three, we obtained the best condition settings for plunging the sample with Vitrobot, developed some special procedures for mounting and transferring the sample, and made a few anti-contamination devices to reduce the ice accumulation in the chamber. All of this paves the way for the imaging of frozen-hydrated samples. To minimize the ice buildup during data collection, we can make a "cryo box" as mentioned in Chapter Three, shielding the specimen from the environment completely with two little holes in the beam path. This step may ensure us that the scattering from ice buildup will be negligible.

The last problem discussed in this dissertation is the centering of the data. When the center of the data is not the true zero spatial frequency position, a linear ramp will enter into the reconstruction of the phase. When this misalignment is three pixels or more, the reconstructed phase may be seriously

wrapped. Even a couple of pixels misalignment in each 2D data may result into a distorted 3D data cube when assembled together. In Chapter Four, we presented a method to find the zero spatial frequency position in the data accurately. This method involves three independent steps. We first use the power spectrum of the diffraction pattern to pre-align the data, which in most cases reduces the misalignment to no more than a couple of pixels. We then minimize the imaginary part in the autocorrelation of the data, which will further reduce the misalignment to within one pixel. With such a data, a reasonable reconstruction of the phase can be obtained without wrapping. We finally make use of the phase ramp present in the reconstruction to precisely align the center of the data to its zero spatial frequency position. This procedure is not included in "Merger," the data assembly software previously used in the group; however, it would be useful to add it into its cousin "Commie," which is being developed.

The journey towards frozen-hydrated specimens has been challenging, but with more and more problems being discovered, and more and more of them being solved, a promising reconstruction may be obtained in the near future.

Appendix A

Interlock

Initially our apparatus had a manual valve VVR5 between the beamline and our chamber. It was necessary to close it "manually" during sample insertion or removal so that if the goniometer airlock valve did not seal the beamline would not get vented. However, this procedure was not always followed so that a few vacuum accidents occurred (coincidentally, always in the wee hours in the morning). Forgetting closing the manual valve may result breaking the Be window and venting the whole ring. To prevent this from happening, we would like to put a automated valve. There are two optical sensors built into our GEOL gomiometer: one senses the pin on the side of the sample holder, and the other senses the flag at the end of the sample holder. We can make use of the signals from these two sensors to control the opening and closing of the valve. All we need to do is to get the signals, and build a logic circuit in the interlock – either the Omron one we are using for controlling the facilities in the main chamber or the one from ALS. (For details on the Omron controller, see: http://xray1.physics.sunysb.edu/∼micros/diffmic_expt/diffmic_expt.html)

The new interlock system only looks at the flag signal: only when the flag is blocked, and pressure in the main chamber and the interlock is good, will we allow the valve VVR5 to be opened. This require the sample holder to be in even when one is not looking at samples, such as aligning the beam. If necessary, we could even manufacture a fake short "sample holder": a cylinder to seal the o-ring in the interlock chamber to allow pumping down.

The goniometer photo-interrupter signal is picked up by the motor amplifier. We need an interface box to take the 5V signal from the motor amplifier and output a 24V signal for the ALS EPS system. Fig. A.1 is the original drawing of the motor amplifier board for goniometer. Fig. A.2 is the circuit of the interface box built by Chuck Pancake and me. Fig. A.3 is the board layout of the box. Inside the box we have two identical sets of circuits, one for the flag signal, the other for the pin signal. Currently the pin signal is not used.

The power used in all ALS interlocks is 24 VDC, while the optical interruptor is driven by 5 VDC. Therefore we starts with 24 VDC signal level, used capacitors to stabilize the signal, and used a LM780-5 voltage power regulator to obtain 5 VDC. Another capacitor is connected to the output of the power convertor to stabilize the 5 VDC signal. Other elements used in the circuits includes:

1. Optical interruptor: Sharp GP1S59 (DigiKey part 425-1058-5-ND).

2. Resistors: R1 = 4.02 KΩ, R2 = 182 Ω.

3. Diodes: D1 and D2 are 1N914, D3 is 1N4001.

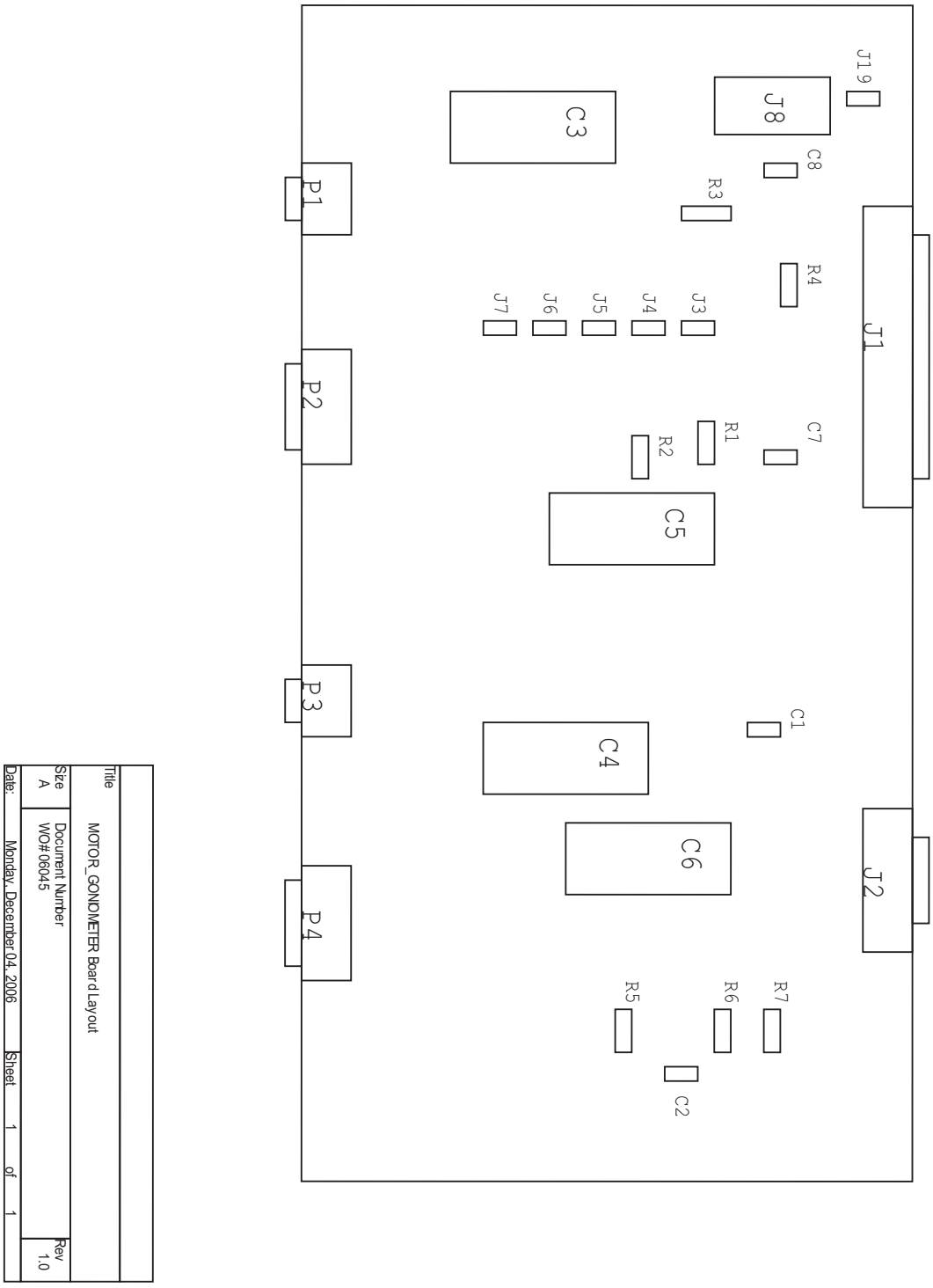

Figure A.1: Physical layout of the goniometer motor amplifier board.

4. Transistor: Q1 is 2N3904.

5. Relay: single-pole dual-toggle, Potter and Brumfield part RY210024 (DigiKey part PB994-ND).

When the optical sensor is not blocked, the relay will not be energized, so that COM is connected to NC (normally closed). When the optical sensor is blocked, COM is connected to NO (normally open).

We also re-wired the photo-interrupters and modified the motor-amplifier board, as shown in Fig. A.4.

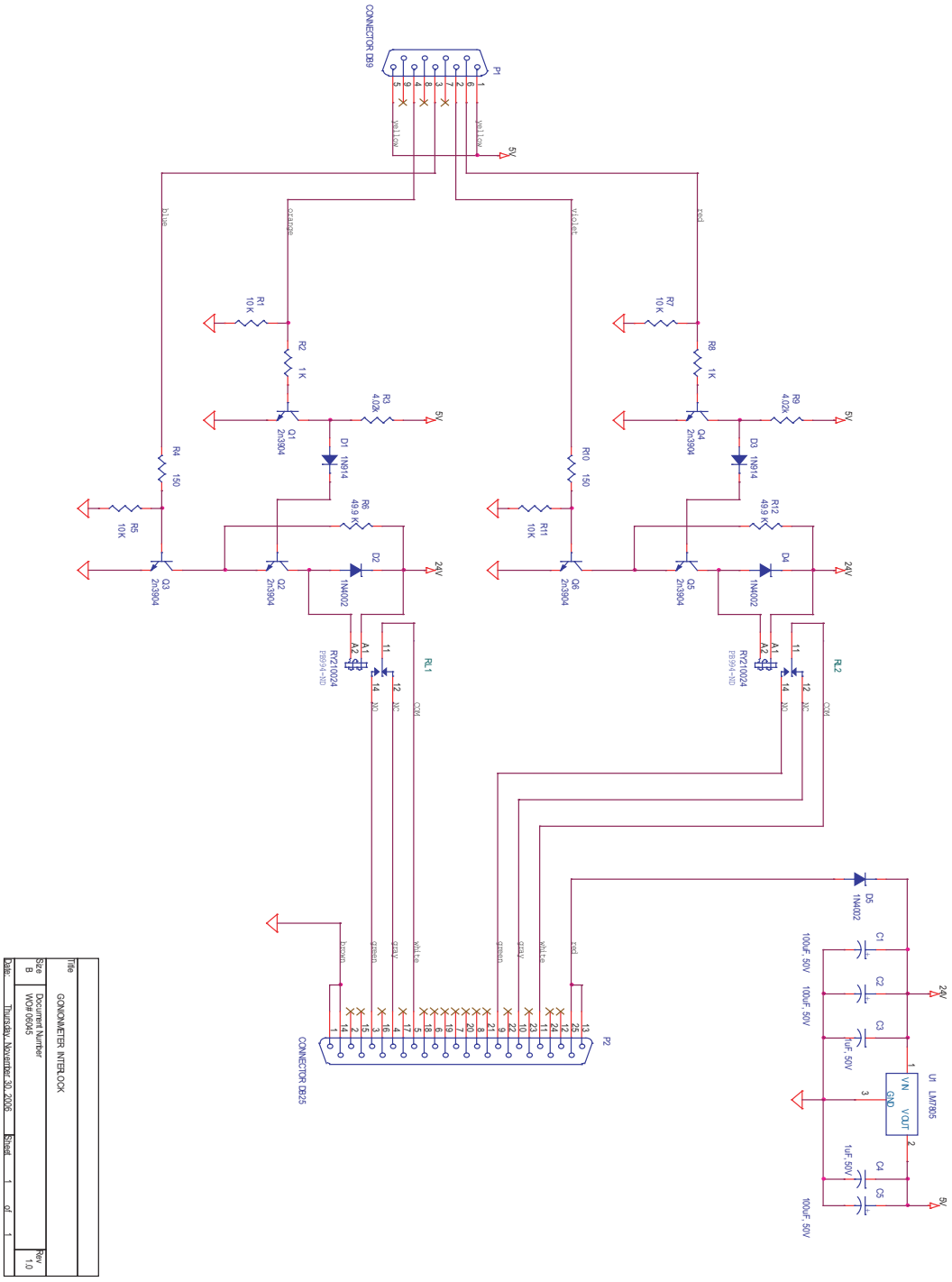

Figure A.2: Circuit of the interface box

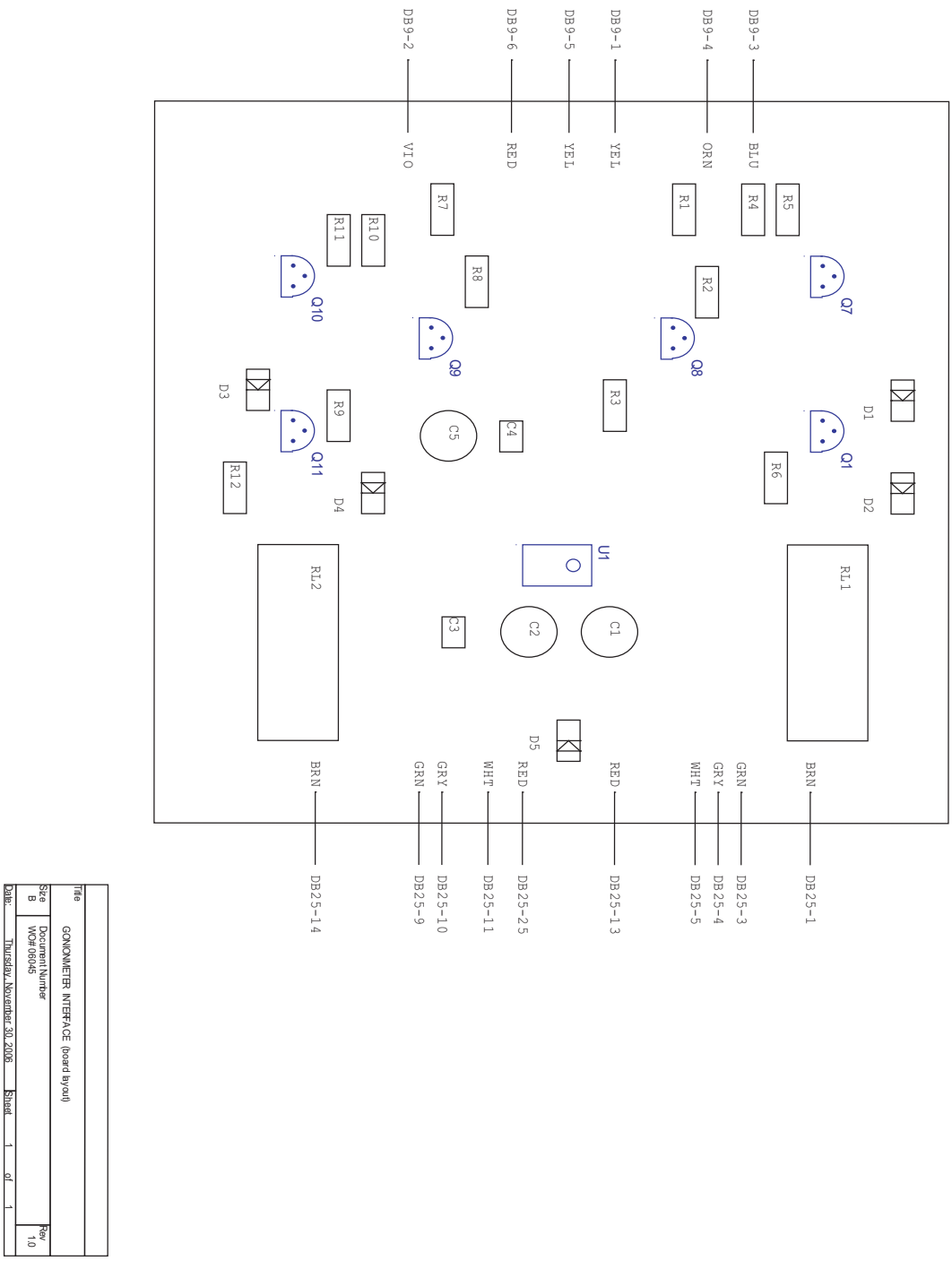

Figure A.3: Board layout of the interface box

Figure A.4: Photo-interrupter wiring

Bibliography

[1] M. Wilkins. The molecular configuration of nucleic acids. *Nobel Lecture*, December 11, 1962, 1962.

[2] H. Chapman-C. Cui J. Holton C. Jacobsen J. Kirz E. Lima S. Marchesini H. Miao D. Sayre D. Shapiro J. Spence M. Howells, T. Beetz. An assessment of the resolution limitation due to radiation-damage in x-ray diffraction microscopy. *Submitted to J. Elec. Spec. and Related Phenomena*, 2004.

[3] J. Steinbrener-J. Nelson A. Stewart D. Shapiro C. Jacobsen X. Huang, H. Miao. Signal to noise considerations in diffraction and conventional microscopy. To appear.

[4] R. Glaeser. *Radiation Damage and Biological Electron Microscopy*. Wiley, 1968.

[5] D. Sayre, J. Kirz, R. Feder, D. M. Kim, and E. Spiller. Transmission microscopy of unmodified biological materials: Comparative radiation dosages with electrons and ultrasoft x-ray photons. *Ultramicroscopy*, 2: 337–341, 1977.

[6] N. Bershad and A. Rockmore. On estimating signal-to-noise ratio using the sample correlation coefficient. *IEEE Transactions on Information Theory*, pages 112–113, 1974.

[7] J. Goodman. *Introduction to Fourier Optics*. McGraw-Hill, 1996.

[8] D. Sayre. Some implications of a theorem due to shannon. *Acta. Cryst.*, 5:843, 1952.

[9] H. Hauptman and J. Karle. Solution of the phase problem. i. the centrosymmetric crystal. *ACA monograph No. 3 (Edwards: Ann-Arbor, USA)*, 1953.

[10] W. Cochran and S. Carroll. A sampling investigation of the efficiency of weighting inversely as the estimated variance. *Biometrics*, 9:447–459, 1953.

[11] J. Karle. Recovering phase information from intensity data. *Nobel Lecture*, 1985.

[12] D. Sayre. Prospects for long-wavelength x-ray microscopy and diffraction. In M. Schlenker, editor, *Imaging Processes and Coherence in Physics*, pages 229–235. Springer-Verlag, Berlin, 1980.

[13] J. R. Fienup. Reconstruction of an object from the modulus of its fourier transform. *Optics Letters*, 3(1):27–29, 1978.

[14] J. Miao, D. Sayre, and H. N. Chapman. Phase retrieval from the magnitude of the Fourier transforms of non-periodic objects. *Journal of the Optical Society of America*, A 15(6):1662–1669, 1998.

[15] J. Miao, P. Charalambous, J. Kirz, and D. Sayre. An extension of the methods of x-ray crystallography to allow imaging of micron-size non-crystalline specimens. *Nature*, 400:342–344, 1999.

[16] G. Williams-M. Pfeifer J. Pitney I. Robinson, I. Vartanyants. Reconstrution of the shapes of gold nanocrystals using coherent soft x-ray diffraction. *Physics Review Letters*, 87(19):195505–1, 2001.

[17] J. Miao, T. Ohsuna, O. Terasaki, K.O. Hodgson, and M.A. O'Keefe. Atomic resolution three-dimensional electron diffraction microscopy. *Physical Review Letters*, 89:155502, 2002.

[18] M. Howells-U. Weierstall G. Hembree J. Spence H. He, S. Marchesini. Experimental lensless soft x-ray imaging using iterative algorithms: phasing diffuse scattering. *Acta Crystal. Sec. A*, 69:143–152, 2003.

[19] Barty A. Marchesini S.-Noy A. Hau-Riege S. Cui C. Howells M. Rosen R. He H. Spence J. Weierstall U. Beetz T. Jacobsen C. Chapman, H. and D. Shapiro. High-resolution ab initio three-dimensional x-ray diffraction microscopy. *JOURNAL OF THE OPTICAL SOCIETY OF AMERICA A-OPTICS IMAGE SCIENCE AND VISION*, 23:1179–1200, 2006.

[20] D. Shapiro and etc. Biological imaging by soft x-ray diffraction microscopy. *PNAS*, 102(43):15343–15346, 2005.

[21] W. Saxton R. Gerchberg. A practical algorithm for the determination of phase from image and diffraction plane pictures. *Optik*, 35:237–246, 1972.

[22] J. Fienup. Phase retrieval algorithm: a comparison. *Applied Optics*, 1982.

[23] R. Lyon D. Luke, J. Burke. Optical wavefront reconstruction: Theory and numerical methods. *SIAM Rev.*, 44:169–224, 2002.

[24] V. Elser. Phase retrieval by iterated projections. *Journal of the Optical Society of America*, A20(1):40–55, 2003.

[25] M. Oxley-D. Paganin H. Faulkner, L. Allen. Computational aberration determination and correction. *Opt. Comm.*, 216:89–98, 2003.

[26] S. Hau-Riege H. He-S. Marchesini J. Spence W. U M. Howells, H. Chapman. X-ray microscopy by phase-retrieval methods at the advanced light source. *Journal de Physique IV*, 2003.

[27] G. Peix-J. Baruchel F. Peyrin M. Schlenker C. PateryronSalome, J. Buffiere. Observation of microstructure and damage in materials by phase sensitive radiography and tomography. *J. Appl. Phys.*, 81:5878–5886, 1997.

[28] S. Fiedler-A. Bravin P. Coan J. Baruchel J. Hartwig W. Thomlinson E. Pagot, P. Cloetens. *Appl. Phys. Let.*, 82:3421–3423, 2003.

[29] D. Paganin-S. Wilkins T. Weitkamp A. Snigirev C. Rau I. Snigireva H. Youn I. Dolbnya W. Yun B. Lai R. Garrett D. Cookson K. Hyodo M. Ando A. Stevenson, T. Gureyev. Phase-contrast x-ray imaging with synchrotron radiation for materials science applications. *Nucl. Instrum. & Meth. Phys. Res. B*, 199:427–435, 2003.

[30] C. Giacovazzo-B. Carrozzini G. Cascarano H. Padmore J. Spence, J. Wu.

Solving non-periodic structures using direct methods: phasing diffuse scattering. *Acta Crystal. A*, 59:255–261, 2003.

[31] Kremer McIntosh OToole, Wray. *Journal of Struct. Bio*, 110:55, 1993.

[32] U. Weierstall J. Spence and M. Howells. Coherence and sampling requirements for diffractive imaging. *Ultramicroscopy*, 101:149–152, 2004.

[33] E. Scheidmiller-M. Yurkov G. Geloni, E. Saldin. Transverse coherence properties of x-ray beams in third-generation synchrotron radiation sources. *Submitted to Elsevier Science*, 2008.

[34] Born and Wolf. *Principles of Optics: Electromagnetic Theory of Propagation, Interference and Diffraction of Light.* Cambridge University Press, 1999.

[35] R. Coisson and S. Marchesini. Gauss-schell sources as model for synchrotron radiation. *Journal of Synchrotron Radiation*, 4:263–266, 1997.

[36] K. Kim. Brightness, coherence and propagation characteristics of synchrotron radiation. *Nuclear Instruments and Methods in Physics Research*, A246:71–76, 1986.

[37] H. He-S. Marchesini J. Spence M. Howells, P. Charalambous. An off-axis zone-plate monochromator for high-power undulator radiation. *Proc. of SPIE*, 4783:65–73, 2002.

[38] T. Beetz. *Soft x-ray diffraction imaging with and without lenses and radiation damage studies.* PhD thesis, Stony Brook University, 2004.

[39] Als storage ring parameters, 2004. URL http://www-als.lbl.gov/als/techspecs/srparameters.html.

[40] B. Henke. Ultrasoft x-ray microscopy. In G. L. Clarke, editor, *The Encyclopædia of Microscopy*. Rienhold, New York, 1961.

[41] A. Roberts-S. Flewett A. Peele D. Paterson M. de Jonge K. Nugent C. Tran, G. Williams. Experimental measurement of the four-dimensional coherence function for an undulator x-ray source. *Physics Review Letters*, 98:224801, 2007.

[42] E. Anderson-D. Attwood C. Chang, P. Naulleau. Spatial coherence characterization of undulator radiation. *Optics Communications*, 182:25–34, 2000.

[43] M. Howells. Optical designs and tolerances for the 8.3.1 protein crystallography beam line, 1999. URL http://xraysweb.lbl.gov/pxbeamline/PX%20philosophy%20paper.pdf.

[44] M Mller RA Steinbrecht. *Cryotechniques in Biological Electron Microscopy*. Springer, 1987.

[45] D. Shapiro. *Biological imaging by soft x-ray diffraction microscopy*. PhD thesis, Stony Brook University, 2004.

[46] J. Kirz, C. Jacobsen, and M. Howells. Soft x-ray microscopes and their biological applications. *Quarterly Reviews of Biophysics*, 28(1):33–130, 1995. Also available as Lawrence Berkeley Laboratory report LBL-36371.

[47] S. Gruner C. Kim, R. Kapfer. High-pressure cooling of protein crystals without cryoprotectants. *Acta Crystl. D*, 61:881–898, 2005.

[48] E. Lima. *The advancement of biological imaging through x-ray diffraction microscopy*. PhD thesis, Stony Brook University, 2006.

[49] J. Pulokas-C. Potter B. Carragher A. Cheng, D. Fellmann. Does contamination buildup limit throughput for automated cryoem? *Journal of Structural Biology*, 154:303–311, 2006.

[50] Elser V. Jacobsen C.-Shapiro D. Tibault, P. and D Sayer. *Acta Cryst.*, 62:248–261, 2006.